AGU ADVANCING EARTH AND SPACE SCIENCE

Water Resources Research®

Key Points:

- New soil column experiments illustrate joint redox potential and soil saturation dynamics
- A novel computational model is able to explain redox potential dynamics
- Saturation velocity exerts a major control on the cycles of redox potential

Spatially Explicit Linkages Between Redox Potential Cycles and Soil Moisture Fluctuations

Filippo Miele[1], Paolo Benettin[1] ![ORCID], Simiao Wang[2], Ivan Retti[2], Mitra Asadollahi[1] ![ORCID], Manon Frutschi[2], Binayak Mohanty[3] ![ORCID], Rizlan Bernier-Latmani[2], and Andrea Rinaldo[1,4] ![ORCID]

[1]Laboratory of Ecohydrology ENAC/IIE/ECHO, École Polytechnique Fédérale de Lausanne, Lausanne, Switzerland, [2]Environmental Microbiology Laboratory ENAC/IIE/EML, École Polytechnique Fédérale de Lausanne, Lausanne, Switzerland, [3]Department of Agricultural and Biological Engineering, Texas A & M University, College Station, TX, USA, [4]Dipartimento ICEA, Università degli studi di Padova, Padova, Italy

Abstract Reduction-oxidation cycles measured through soil redox potential (E_h) are associated with dynamic soil microbial activity. Understanding changes in the composition of, and resource use by, soil microbial communities requires E_h predictability under shifting hydrologic drivers. Here, 50-cm soil column installations are manipulated to vary hydrologic and geochemical conditions, and are extensively monitored by a dense instrumental deployment to record the depth-time variation of physical and biogeochemical conditions. We contrast measurements of E_h, soil saturation and key compounds in water samples (probing the majority of soil microbial metabolisms) with computations of the relevant state variables, to investigate the interplay between soil moisture and redox potential dynamics. Our results highlight the importance of joint spatially resolved hydrologic flow/transport and redox processes, the worth of contrasting experiments and computations for a sufficient understanding of the E_h dynamics, and the minimum amount of biogeochemistry needed to characterize the dynamics of electron donors/acceptors that are responsible for the patterns of E_h not directly explained by physical oxic/anoxic transitions. As an example, measured concentrations of sulfate, ammonium and iron II suggest coexistence of both oxic and anoxic conditions. We find that the local saturation velocity (a threshold value of the time derivative of soil saturation) exerts a significant hysteretic control on oxygen intrusion and on the cycling of redox potentials, in contrast with approaches using a single threshold saturation level as the determinant of anoxic conditions. Our findings improve our ability to target how and where hotspots of activity develop within soil microbial communities.

Plain Language Summary Redox potentials measured in a set of lysimeter experiments for natural soil columns were contrasted by depth-time computations to single out the actual controls on redox cycling. Our results show that the dynamics of soil saturation is not always directly linked to oxic/anoxic transitions generating the kind of changes in the reducing or oxidizing conditions that require adaptations by soil microbial communities. In particular, the rate of change imposed to the hydrologic forcings proves to be a key and so far unrecognized actor. We believe that our results will prove important because pre-requisites are established for understanding the adaptation of soil microbial communities in response to shifts in hydrologic drivers—whose scenarios are arguably predictable.

1. Introduction

A key challenge for contemporary ecohydrology lies in understanding how different ecosystems respond to shifting water availability, and in identifying how hydrologic and climatic drivers mold the selective pressures shaping living communities (Porporato & Yin, 2022; Rinaldo et al., 2020; Rodriguez-Iturbe & Porporato, 2005). Microbial communities are key players in global biogeochemical cycles (Falkowski et al., 2008), regulating ecosystem function (Borer & Or, 2021; Gibbons & Gilbert, 2015). Hydrological processes in soils are known to drive shifts in microbial activity (e.g., Magnabosco et al., 2018; Rillig et al., 2017; Zhang & Furman, 2021), forcing conditions that lead to local variations in the availability of oxygen and electron donors. Thus, hydrology contributes to determining transitions between oxic and anoxic conditions and, consequently, to delineating the zones in which soil redox potential (E_h) fluctuations occur. Zones characterized by highly dynamic oxic/anoxic transitions are potential hotspots for change in soil microbial communities (Magnabosco et al., 2018). In this context, the ultimate goal of this experimental and theoretical study is to focus on the soil microbial activity that may

Methodology: Filippo Miele, Paolo Benettin, Simiao Wang, Mitra Asadollahi, Manon Frutschi, Binayak Mohanty, Rizlan Bernier-Latmani, Andrea Rinaldo
Project Administration: Andrea Rinaldo
Resources: Paolo Benettin, Simiao Wang, Ivan Retti, Manon Frutschi, Rizlan Bernier-Latmani, Andrea Rinaldo
Software: Filippo Miele, Mitra Asadollahi
Supervision: Paolo Benettin, Rizlan Bernier-Latmani, Andrea Rinaldo
Validation: Filippo Miele, Paolo Benettin, Simiao Wang, Mitra Asadollahi, Manon Frutschi
Visualization: Filippo Miele, Simiao Wang
Writing – original draft: Filippo Miele, Rizlan Bernier-Latmani, Andrea Rinaldo
Writing – review & editing: Filippo Miele, Paolo Benettin, Binayak Mohanty, Rizlan Bernier-Latmani, Andrea Rinaldo

be explained in terms of hydrological controls on reduction-oxidation (redox) cycles (Aller et al., 2010; Ginn et al., 2017; Magnabosco et al., 2018; Richaume et al., 1989; Rillig et al., 2017; Soucy et al., 2015).

It has been recently observed (Huang et al., 2021) by reviewing existing data sets (Moyano et al., 2012; Wang et al., 2014; Yan et al., 2018) that spatially lumped soil microbial respiration rates are directly shaped, in the long term, by the stochastic features of water injection (say, described by marked Poisson processes through mean intensity of daily precipitation and mean interarrival of rainy days (Rodriguez-Iturbe et al., 1987)) under the critical assumption that timescales of soil moisture changes are longer than those controlling the response of the microbial community. Understanding the environmental conditions that prompt rapid shifts in microbial activity is assumed here to require not only descriptions of the hydrologic stress and their related sequences of oxic/anoxic conditions, but also a comprehensive view of biogeochemical drivers of the resulting redox potential. In a nutshell, soil wetness remains essential in shaping bacterial abundance, dispersal and function (e.g., Bickel & Or, 2021; Federle et al., 1986; Hazen et al., 1991; Scheidweiler et al., 2020) but decisive co-factors emerge.

Here, we seek to characterize how transport phenomena and soil moisture fluctuations, typical of soil columns and observable within experimental lysimeters, allow for spatially explicit temporal determinations of the drivers and the extent of redox fluctuations. Specifically, by coupling the experimental determination of soil saturation with extensive biogeochemical measurements, we study the role of the hydrologic dynamics in the making of the patterns of redox potentials to probe whether assumptions feasible for bulk soil respiration (Huang et al., 2021) prove vialble. Additionally, a coupled transport/biogeochemical model of unsaturated porous media was developed for the interpretation of the experimental data. Measurements of the microbial community composition would require extensive sampling and analysis of soil and water, resulting in an invasive and costly field methodology. Instead, direct measurements of soil redox potential, coupled with chemical analyses of pore water samples, prove a much less invasive and a more efficient way to monitor microbial activity (Rodríguez-Escales et al., 2020). Despite being less invasive than the characterization of the microbial community, spatially and temporally resolved E_h measurements remain a major effort, much more so than the measurement of soil moisture content. Thus, a key task for the present analysis is to investigate whether the determination of the dynamics of soil saturation would suffice in characterizing redox cycles (e.g., Borer et al., 2018; Ebrahimi & Or, 2015; Tecon & Or, 2017). We address how redox regimes vary when subjected to a spatial gradient of carbon sources (e.g., Magnabosco et al., 2018; Simkus et al., 2016) in conjunction with shifts in the depth of soil saturation due to controlled water application and drainage regimes (e.g., Benettin et al., 2021; Queloz et al., 2015).

Here, we present a set of novel experiments in which relatively large soil columns (diameter 30 cm, depth 50 cm) are subjected to controlled wetting/draining cycles and soil saturation, and E_h values are monitored to high depth-time resolution. Our aim is to determine to what extent the redox potential response of soil under fluctuating soil moisture contents can be described based simply on soil water content. A parsimonious compartmental model of the relevant transport processes, tailored to the experimental setup available, was also developed to add a proper biogeochemical context.

The paper is organized as follows. A Methods collection (Section 2) provides (a) a brief description of the experiments carried out, where most technical details are referred to the Supporting Information S1 (Section 2.1), followed by (b) a detailed analysis of the computational tools developed to contrast the experimental figures. Specifically, Section 2.2 describes the spatially explicit flow and transport models developed, and the rationale underpinning the computation of time-dependent redox potentials. Then, Section 3 presents a synoptic view of experimental and computational results, followed by Section 4 that includes, in particular, a discussion on limits and validity of the experimental setups and of the models utilized. A set of conclusions (Section 5) recapitulates our main findings and their relevance.

2. Methods

2.1. Experimental Design

To decipher the spatial-temporal responses of the redox potential to fluctuations in soil saturation, we conducted water application-drainage experiments differing in terms of the induced extent of saturation periods and of the rapidity of the variations imposed. These experiments were also characterized by variable spatial density of the measuring devices (Figure 1). All the experiments were carried out in large (30-cm diameter, 50-cm height) laboratory soil columns, filled with preteated loamy soil (Schroth et al., 1995) from a forest site near Lausanne (Switzerland) and irrigated from the top through a controlled shower system (Supporting Information S1).
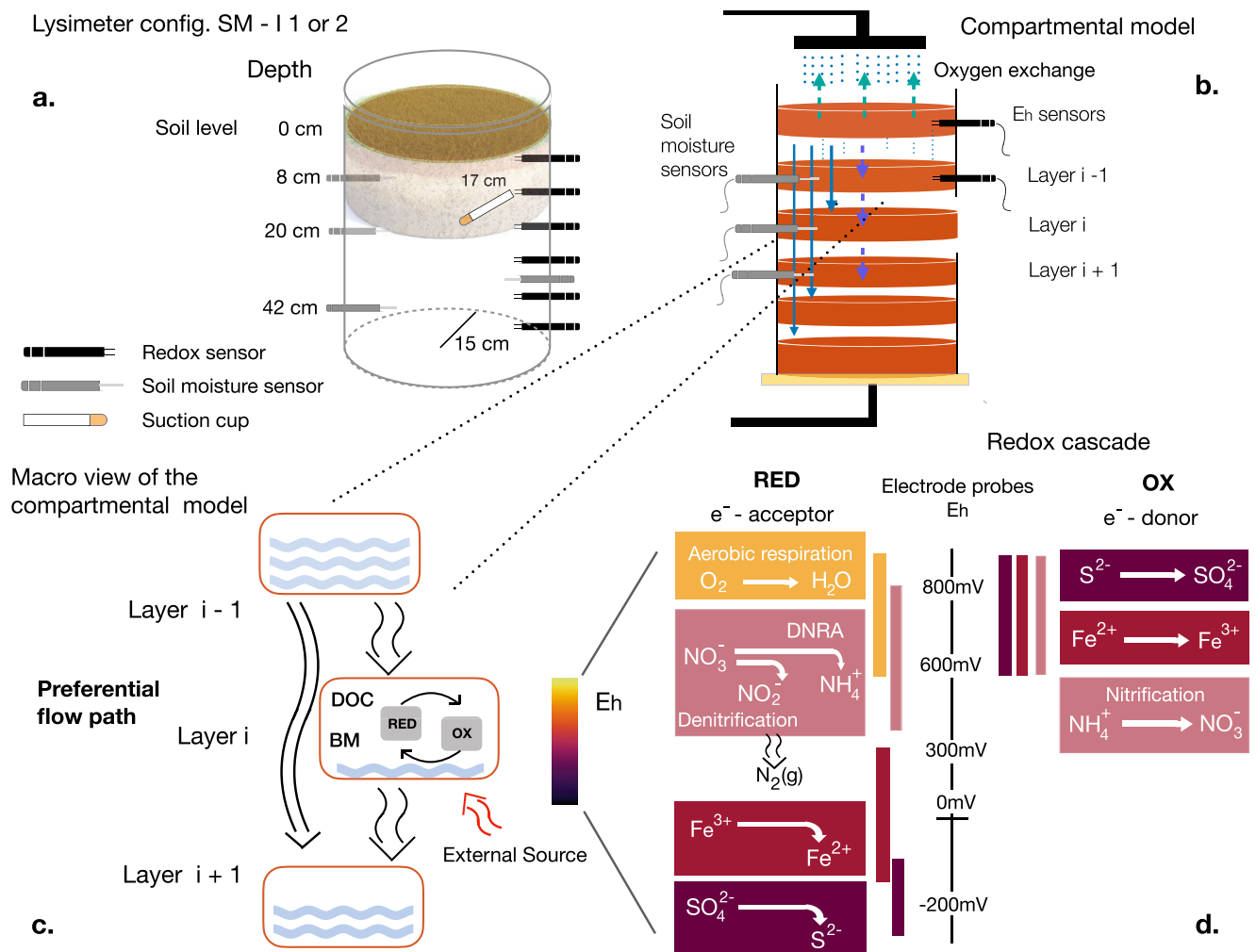
Figure 1. (a) Lysimeter setups for experiments SM-I1/SM-I2 (see Supporting Information S1 for details). (b) Lysimeter schematic. The system is composed of a PVC column of 30-cm diameter and ~50-cm depth, a shower on the top and a vacuum pressure pump at the bottom (see Supporting Information S1 for details). (c) The compartmental model simulates the dynamic within as a sequence of connected layers. In each layer i, the three processes of transport T^i, source S^i and reaction R^i, described by Equations 2 and 3, take place. The overall reaction term is decomposed according to the redox processes triggered by the activity of the microbial biomass (BM) that contribute to the evolution of the redox potential E_h. The system cyclically alternates between states referred to as RED and OX (listed in panel d.)) depending on the relative presence of oxygen. The presence of preferential flow paths potentially connects each layer with any other layer. (d) Redox ladder for the biogeochemical process considered in this work. On the left, the range of soil redox zonations (at pH 7.5 and 25 T°) refers to the redox pairs values where the oxidizer (electron acceptor, left side of reaction) is reduced under anaerobic condition. On the right side, the redox range of the electrode probes where the electron donor is oxidized back under aerobic conditions (e.g., Anderson, 2005; Rodríguez-Escales et al., 2020; Stumm & Morgan, 1996a; Zhang & Furman, 2021).

In many forest environments, rainfall is the only available hydrological flux and organic carbon amendment is mainly represented by litterfall in the topsoil. Real-world precipitation patterns are known to be a stochastic process at daily timescales that can be described in terms of marked Poisson point processes (Rodriguez-Iturbe & Porporato, 2005; Rodriguez-Iturbe et al., 1987) parametrized by two relevant quantities: the mean interarrival time between two events, and the mean precipitation intensity of each event, whose product defines the mean of the process. However, adopting such rainfall patterns would introduce a further level of uncertainty in the response of the soil microbial activity. Instead, here we seek to focus on the shifts in microbial activity and soil saturation dynamics rather than on the effects of irregular rainfall regimes. As a result, we opted for setting up regular water application-drainage cycles, leaving the option to explore a more complex scenario as a logical follow-up of this work.

Due to the limited number of slots available in any lysimeter, each experimental set-up has been thought to provide a good trade-off among the possible measurements (pore-water samples, tension, soil moisture and redox

potential). A brief overview of the experimental setups and their measurements is provided below (further details are reported in the Supporting Information S1):

- SM-B experiment: In this case, the slots available along the vertical direction have been used to measure Eh values (at six different depth) and collect pore water samples, thus, no soil moisture sensors were installed. The experiment, was carried out by filling the bottom 40 cm of the column with forest soil and the top 15 cm with a mixture of leaves and soil (at a leaf:soil ratio of 1.6:1 by mass). The bottom of the column was gravity-drained through and the bottom of an open funnel;

- Experiments SM-I1 and SM-I2: Two other experiments were soil saturation-informed. In both, the organic carbon source was dissolved in the rainwater solution, and soil moisture sensors were placed along the vertical direction along with redox potential electrodes. The bottom drainage was controlled through a suction pump. The lysimeter configuration in these two cases, has been chosen to prefer a vertical monitoring of the soil moisture and reduce the water samples to the only bottom position. The experiments differed in terms of the duration of saturation/desaturation cycles: in SM-I1, the water application and bottom drainage were controlled to achieve week-long saturation periods alternating with rapid, day-long drainage and re-saturation; in SM-I2, a regular regime of daily precipitation and a fixed bottom suction pressure were used to establish daily moisture cycles;

- Additionally, in SM-I2, a single pulse injection of nitrate was applied to input water to identify the impact of soil moisture fluctuations on the fate and transport of nitrate;

In all the experiments, the lysimeter was filled with the same type of soil, whose native total organic carbon (TOC) was measured to be around 1.3% (see Sections S1 and S4 in Supporting Information S1 and (Gubler et al., 2019; Guillaume et al., 2022)). To drive microbial processes in SM-B, additional organic carbon was provided by the mixture of soil and leaves. The latter reported a native TOC level around 25%. In SM-I 1 and 2, additional carbon was supplied in the form of dissolved organic carbon (DOC), directly added in the applied solution (see Section S4 in Supporting Information S1). The lysimeter has been packed with the following procedure: 0–15 cm depth with 2.25 kg of soil/leaf mixture per 5 cm and 15–65 cm depth with 4.5 kg soil each 5 cm.

The measured redox potentials (E_h) are reported against the silver chloride electrode (Ag/AgCl) reference, and are extensively used to contrast theoretical predictions. Thus, when compared to E_h measurements detected with different instruments, each value must be positively shifted by 205 mV, considering a room temperature of 25°.

2.2. Spatially Explicit Compartment Model for Reactive Transport

Closed mass-balance formulations to model soil moisture-driven redox reactions such as oxygen, nitrogen and iron reduction have previously been developed at the level of a spatially implicit single bioreactor (e.g., Calabrese & Porporato, 2019; Manzoni & Porporato, 2007; Rubol et al., 2013). Key to these formulations is that hydrological processes are treated as spatially lumped, and the soil moisture dynamics are brought back to the balance of precipitation, evapotranspiration and leakage. Referring to a generic redox-couple *A/B*, in which *A* is the oxidized form (able to accept electrons) and *B* is the reduced form (able to donate electrons), the redox potential dynamics are governed by the time evolution of the concentrations C_A and C_B, which is kinetically driven by reducing and oxidizing rates.

To interpret the experimental data, here we set up a one-dimensional layered/compartment model that simulates reactive transport phenomena to describe quantitatively the spatio-temporal behavior of the redox potential (E_h, defined in Section 2.2.3) along a vertical transect of a soil profile (Figure 1). We investigate the interplay between soil moisture dynamics and patterns of E_h in columns of natural soils artificially irrigated and drained by targeting the dominant redox reactions in space and time.

Each simulated soil layer is tailored to match the position of specific redox probes in our experimental lysimeters. Within each layer, the concentrations of biomass (BM), DOC and terminal electron acceptors (TEAs) are integrated over time according to the expected reactions within any given layer, as well as to possible sources/sinks and flux exchanges between connected layers (whether adjacent or not, such as connections arising because of preferential flow paths). Effective soil and hydraulic parameters were manually calibrated (SI) to simulate soil moisture dynamics and internal fluxes as well as kinetic rates to describe electron acceptor dynamics. The model allows us to quantitatively assess how sensitive redox potential changes are to variations in soil saturation.

We describe the temporal evolution of the stored mass M_A^i (expressed in mM per unit area) of a redox species A within layer i through a general mass balance scheme that is,:

$$\frac{d M_A^i}{dt} = R_A^i + S_A^i + T_A^i \tag{1}$$

where the terms R and S are respectively reaction and source/sink terms (Section 2.2.1), while T accounts for the mass transport across layers (Section 2.2.2). Solution to Equation 1 allows us to compute the redox potential at each layer (Section 2.2.3). While this Methods section establishes the general formulation of the equations, details of their application to our three case studies are reported in the Supporting Information S1 Appendix.

2.2.1. Implementation of Redox Reactions

To describe the redox reactions, we follow an established compartmental description for reversible reactions (Calabrese & Porporato, 2019; Manzoni & Porporato, 2007), which is similar to Equation 1 for a single layer except for the transport term. Central in the redox processes is the requirement that the transfer of electrons occurs from an electron donor to an electron acceptor, fueling energy generation. In microbial organotrophic metabolism, organic compounds serve as the electron donor, and the oxidation is coupled to the reduction of a diversity of electron acceptors. Thus redox processes are triggered by the consumption of soil organic carbon (SOC).

We define the reactions of A and B by considering the second (complementary) half-reaction. Species A serves as the TEA in an organotrophic metabolism that results in the consumption of organic carbon. It is thus reduced to species B. Alternatively, B may serve as an electron donor, delivering electrons to O_2. Species B can be readily oxidized back to A due to its tendency to donate electrons through either abiotic or biotic oxidation. Thus, the half-reactions involved in each redox couple can be complemented as follows:

$$CH_2O + A \Rightarrow CO_2 + B \tag{2}$$

$$B + O_2 \Rightarrow A + H_2O \tag{3}$$

where the reduction of A is coupled to the consumption of organic carbon that serves as the electron donor (unbalanced Equation 2) and the oxidation of B (referred as OX_B) is coupled to the depletion of O_2 (unbalanced Equation 3).

Soil saturation $0 \geq s \geq 1$ plays a pivotal role in constraining redox reactions. In agreement with what is observed by Daniels (2016) (see also (Ray & Nyle, 2017)) and formulated by Calabrese and Porporato (2019) and by Rubol et al. (2013), low soil moisture levels limit the reduction rate of non-oxygen electron acceptors because high oxygen concentrations suppress anaerobic microbial processes and the transport of dissolved chemicals is physically inhibited. In their work, the soil anaerobic reduction rate in low-oxygen condition (below/above field capacity s_{fc}) is expressed through the following analytical form

$$f(s) = \begin{cases} 0 & \text{if } s \leq s_{fc} \\ \left(\dfrac{s - s_{fc}}{1 - s_{fc}}\right)^{\beta} & \text{if } s > s_{fc} \end{cases} \tag{4}$$

On the other hand, high saturation levels physically inhibit aerobic respiration, suggesting the use of a function, $g(s)$, that takes oxygen limitation at high saturation into account that is,:

$$g(s) = \begin{cases} 1 & \text{if } s \leq s_{fc} \\ 1 - \left(\dfrac{s - s_{fc}}{1 - s_{fc}}\right)^{\zeta} & \text{if } s > s_{fc} \end{cases} \tag{5}$$

A system of equations equivalent to (4–5) has been used to model nitrogen dynamics including dissimilatory nitrate reduction to ammonium (DNRA) (Rubol et al., 2013) and microbially mediated Fe(II) and Fe(III) cycles in the root zone (Calabrese & Porporato, 2019). We note that the soil field capacity might represent a parameter less relevant then expected for systems that are fluctuating at high saturation levels, where air percolation thresholds may better describe limitations to oxygen diffusion—and thus true oxic/anoxic transitions. Furthermore, it has been shown (Yan et al., 2016) how heterotrophic respiration is explicitly related to the saturation level and

air percolation thresholds at pore scales. Significantly, a polynomial function as expressed by Equations 4 and 5 (thus characterized by a threshold parameter) effectively describes the mechanisms of effective suppression/inhibition of metabolic rates driven by soil moisture levels. To avoid any possible ambiguity, we will replace s_{fc} with a "ritical saturation level" parameter (s_c) in what follows.

The time evolution of the concentration of species A is empirically described by the kinetic rate R_A that stems from the balance between the negative contribution of its reduction rate $\left(\overline{RED_A}\right)$ and the positive contribution to the oxidation rate of its counterpart B (OX_B). The following equation describes mathematically the above process:

$$\frac{dM_A}{dt} = \sum_k R_{A,k} + S_{A,k} = n\, Z_r s \sum_k \left(-\overline{RED}_{A,k} + OX_{B,k}\right) + S_{A,k} \tag{6}$$

$$\frac{dM_B}{dt} = \sum_k R_{B,k} + S_{B,k} = n\, Z_r s \sum_k \left(\overline{RED}_{A,k} - OX_{B,k}\right) + S_{B,k} \tag{7}$$

As the above rates are expressed in units of concentration per unit of water over time, they are multiplied by the water storage $n\, Z_r s$, where s is soil saturation, n is porosity and Z_r is the total depth of the soil column. Note that the index k refers to each of the possible paths that can co-occur in the production (or consumption) of the species. The term S represents any mass source (or sink) that may be associated with for example, mineral dissolution or precipitation.

Due to pore-scale heterogeneities, all reactions can occur simultaneously although with different weights according to (a) the macroscopic oxic/anoxic transitions and (b) the limited mobility of dissolved substrates for dry interstitial regions both driven by soil saturation dynamics.

In this model, organotrophic metabolism results in the reduction of electron acceptor A according to the reduction rate $\overline{RED_A}$. The latter can be expressed by third-order semi-empirical kinetic laws where the reduction associated with the consumption of organic matter, DOC, is catalyzed by the biomass of the microbial population of A-reducers:

$$\overline{RED_A} = f(s)\, k_{red,A} \cdot BM \cdot C_{DOC} \cdot \left(C_A - C_{A_0}\right) \tag{8}$$

where C_A is the species concentrations and C_{A_0} represent the fraction of the species' pool below which metabolism becomes biologically inhibited. An alternative formulation of such biological limiting factors is represented by the non linear Michaelis–Menten rate equation ((Murray, 2002)), in which the role of enzymes is explicitly taken into account. A quantitative comparison between the two formulations may be considered for future work.

On the other hand, lithotrophic metabolism that results in the aerobic oxidation of electron donor B, (OX_B) that is thus converted back to species A, is assumed to be autotrophic. Thus, even if such oxidation rates can be comparable with abiotic oxidation (Roden & Wetzel, 1996; Weber et al., 2006), their impact on biomass build-up is negligible compared to heterotrophic growth. Thus, the oxidation rate will be modeled without taking into account BM and the concentration of organic carbon, as follows (Ginn et al., 2017; Stumm & Morgan, 1996a, 1996b):

$$OX_B = g(s)\, k_{ox,B} \cdot \left(C_B - C_{B_0}\right), \tag{9}$$

where C_{B_0} performs the same function of limiting factor as C_{A_0}.

Equations 2 and 3 are generally suited to describe any reversible redox system such as the one defined by Equation 22. These (unbalanced) equations hold for sulfate reduction/sulfide oxidation, Fe(III) reduction/Fe(II) oxidation and for nitrification/DNRA (dissimilatory nitrate reduction to ammonium) and limits the index k in the summation of Equations 8 and 9 to only these three types of metabolisms. The absence of carbon and nitrogen fixation leaves nitrogen and carbon pathways as open systems where reactions occur only in one direction. The same occurs for O_2 where consumption is due to aerobic respiration while supply is only driven by hydrological processes like oxygen diffusion through unsaturated pores during a drainage phase (see Supporting Information S1, Section 3.1 and (Šimůnek & Suarez, 1993)). Thus, a specific formulation is required for aerobic respiration and for denitrification:

$$\frac{dO_2}{dt} = -RED_{O_2} = -f(s)k_{red,O_2} \cdot BM \cdot C_{DOC} \cdot O_2 \tag{10}$$

while nitrous oxide formation (that precedes nitrogen release through partial denitrification) is represented by:

$$\frac{dN_2O}{dt} \propto (1-\gamma)RED_{NO_3} \tag{11}$$

where γ is the specific weight that balances nitrate consumption through DNRA and denitrification pathways (see Supporting Information S1 Appendix for an explicit formulation of the nitrogen cycle and its balance equation). The related balance equation for DNRA is:

$$\frac{dNH_4}{dt} = \gamma RED_{NO_3} - OX_{NH_4} \tag{12}$$

A more complete description of the complex nitrogen pathways (Maggi et al., 2008), taking into account the dynamics of gaseous phases such as those of intermediate species involved in the reaction, can be implemented in the future.

When focusing on a single anaerobic metabolism (e.g., denitrification, iron reduction, sulfate reduction), the reaction rate is assumed to be constant regardless of the co-occurrence of, and the competition with, other electron acceptors. However, when one seeks to describe the full suite of relevant processes affecting local redox potentials, each redox couple must be studied via a framework that meets the demands of the so-called redox tower hierarchy among TEAs: oxygen first, followed by nitrate, manganese, iron(III), and sulfate. To accomplish this task, each RED_A term is multiplied by a limiting factor ($\Theta_A \in [0, 1]$), $RED_A = \Theta_A \overline{RED_A}$. Such a factor is designed to inhibit the reduction of the electron acceptor within the A/B couple unless all the other more energetically favored e^- acceptors are depleted below a critical value.

Θ_A is described according to Brun and Engesgaard (2002), Rodríguez-Escales et al. (2020):

$$\Theta_A = \prod_{m=1}^{N_A-1} \frac{V_m}{V_m + C_m} \tag{13}$$

where the index C_m indicates the concentration of all the Nth e^- acceptors inhibiting A in being the target terminal electron-accepting process (TEAP). V_m is the inhibiting factor that defines the threshold value below which C_m is too low to be energetically favored and at which the next electron acceptor according to the redox tower hierarchy starts to be reduced. To convince oneself of the previous equation it is enough to consider, for example, how nitrate reduction can be inhibited by oxygen levels: for high oxygen concentrations $\left(C_{O_2} \gg V_{O_2}\right)$ the denominator is larger than the numerator and Θ_{NO_3} tends to zero. When O_2 is depleted to a value much lower than V_{O_2}, C_{O_2} is negligible and Θ_{NO_3} approaches unity. By generalizing to other species, it is clear that sulfide reduction is triggered only if all the prefactors appearing in Equation 13 are close to 1, meaning that all the other energetically favored electron acceptors have been already depleted below a given threshold value. We remark that, although the role of oxygen presence may seem counted twice by the function $g(s)$ and the limiting function Θ_{0_2}, this is not the case. Low saturation levels, especially when monitored in deeper layers, imply reduced diffusivity of dissolved species but do not directly reflect the amount of oxygen that is available (and being consumed).

Finally, the interactions between the microbial community and the organic carbon dynamics is modeled by following a quasi Lotka-Volterra type of equations (Evans & Findley, 1999; Manzoni & Porporato, 2009):

$$\frac{dBM}{dt} = k_{BG}\sum_j RED_j - k_{BD}BM \tag{14}$$

where $j = O_2, NO_3, Fe(III)$ and, SO_4^{2-} as the biomass growth during heterotrophic metabolism has been observed to be proportional to a fraction k_{BG} of the e^- acceptor reduction rates (Lovley (1991), Kostka et al. (2002), Hall et al. (2013), and Roels (1980)) and whereas the second term on the right represents the biomass decay of a fraction of organic carbon produced by biomass degradation, generally considered proportional to the total biomass concentration. It should be noted that the fraction $(1 - k_{BG})$ represents the production rate of CO_2 whose dynamics are not included in the present work. Further, a probabilistic model of biomass growth may be a useful tool to

Table 1
List of Terminal Electron-Accepting Process Reactions; Dissimilatory Nitrate Reduction to Ammonium = Dissimilatory Nitrate Reduction to Ammonia

Process	Model label	Full reaction type	
Organotrophic metabolism			
Aerobic respiration	RED_{O_2}	$CH_2O + O_2 \rightarrow CO_2 + H_2O,$	n_{e^-}: 4
Partial denitrification	$(1 - \gamma)RED_{NO_3}$	$H^+ + NO_3^- + CH_2O \rightarrow 0.5\ N_2O + CO_2 + 1.5\ H_2O,$	n_{e^-}: 4
DNRA	γRED_{NO_3}	$2\ H^+ + NO_3^- + 2\ CH_2O \rightarrow NH_4^+ + 2\ CO_2 + H_2O,$	n_{e^-}: 8
Iron(III) reduction	RED_{Fe}	$0.25\ CH_2O + 0.25\ H_2O + Fe^{3+} \rightarrow Fe^{2+} + 0.25\ CO_2 + H^+,$	n_{e^-}: 1
Sulfate reduction	RED_{SO_4}	$SO_4^{2-} + 2\ CH_2O \rightarrow S^{2-} + 2\ CO_2 + 2\ H_2O,$	n_{e^-}: 8
Lithotrophic metabolism			
Nitrification	OX_{NH_4}	$NH_4^+ + 2\ O_2 \rightarrow NO_3^- + 2\ H^+ + H_2O,$	n_{e^-}: 8
Ferrous oxidation	OX_{Fe}	$Fe^{2+} + 0.25\ O_2 + H^+ \rightarrow Fe^{3+} + 0.5\ H_2O,$	n_{e^-}: 2
Sulfide oxidation	OX_S	$S^{2-} + 2\ O_2 \rightarrow SO_4^{2-},$	n_{e^-}: 8

Note. The second column explicits the terms appearing in Equations 8 and 9. Methanogenesis was not included as no measurements of methane were performed.

reveal ecosystem-scale microbial dynamics (e.g., Huang et al., 2021). However, this is deemed beyond the scope of the present work.

The dynamics of DOC C_{DOC} is then the balance of all the inputs and their consumption that is,:

$$\frac{dC_{DOC}}{dt} = -DEC_{het} + k_{BD}BM + S_{DOC}, \tag{15}$$

where all decay terms (DEC_{het}) come from DOC consumption due to all organotrophic metabolisms, whether happening under aerobic or anaerobic condition:

$$DEC_{het} = \sum_k \nu_k RED_k \tag{16}$$

where ν_k accounts for the stoichiometric coefficient of organic carbon computed by normalizing all the equations in Table 1 via the coefficient of the electron acceptor on the left side of each reaction. In this manner, ν_k represents the fraction of moles of DOC needed to convert 1 mol of the specific electron acceptor. The DOC dynamics presented in our work are a simplification of a more general description (Rubol et al., 2013), where DOC increases by litterfall and depolymerization. The latter converts SOC to DOC as described by a second order differential equation including a decay term proportional to BM. In our case, these are lumped into a single effective source term, S_{DOC} (reported in Table S3 in Supporting Information S1 as 10^{-2}, [mM/day]) that in a first-order approximation neglects large BM fluctuations. The value adopted is consistent, at least within an order of magnitude, with the values reported in the literature (see Table S3 in Supporting Information S1).

2.2.2. Flow and Transport Across Soil Compartments

The discrete set of positions of the soil moisture and redox sensors along the vertical direction enables the description of the soil columns by a layered compartmental model where each sensor location corresponds to the centroid of the representative volume in which reactions take place (Figure 1a). Each soil layer i is characterized by a value of water saturation s^i representing the storage term shaped by input and output water fluxes. The latter may include evaporation, transpiration, capillary rise and percolation. Because our goal is not to reproduce specific field conditions, say by adjusting the bottom boundary conditions in the lysimeters (Groh et al., 2016), but rather to test our ability to capture broad patterns of conditions conducive to soil microbial community adaptations, we focus here only on the main fluxes that are relevant to our experiments, for example, the gravity-driven vertical percolation (L^i) from one layer to the layers below. This downward flux can be related to soil saturation beyond field capacity through the typical polynomial expression (Laio et al., 2001):

$$L^i = -K_{sat}\left(\frac{s^i - s_c}{1 - s_{fc}}\right)^\beta, \tag{17}$$

where s_c is the field capacity, K_{sat} is the saturated hydraulic conductivity and β is an exponent that depends on soil properties (Hornberger et al., 2014). While this formulation is suitable for a gravity-driven flow regime, adaptations are required for different regimes. For laboratory experiments where a bottom suction is applied, the effect of the imposed higher pressure gradient can be modeled by an effective higher $\tilde{K}_{sat} \propto K_{sat} \cdot h_{max}$ where h_{max} is the entry pressure level (see Section S2 in Supporting Information S1), here renamed with the usual K_{sat}. No need arises here to reproduce specific field conditions, which would require special care (Groh et al., 2016).

Soil structure heterogeneity, like the presence of preferential flow paths, may result in a more complex redistribution of the downward flow. To account for this effect, we allow part of the leakage L^i to bypass the layer underneath and be transferred directly to lower layers (see Figure 1b). This is done by splitting the total outflow L^i into subcomponents $q^{i+1,i}$, $q^{i+2,i}$…where $q^{j,i}$ is the flux to layer j from layer i and $\sum_{j>i} q^{j,i} = L^i$. This formulation proves useful in describing transport across scales because preferential flowpaths are not easily defined in terms of classic advection-dispersion transport equations at the continuum scale unless a specific structural model is postulated. The level of detail required by out setup suggests to write the water balance at the layer level, after breaking the leakage term into subcomponents, as follows:

$$n\, Z_r \frac{ds^i}{dt} = \sum_j q^{i,j} - L^i = \sum_j q^{i,j} - \sum_j q^{j,i} \tag{18}$$

where the input flux to the top layer (which corresponds to $q^{1,0}$ in our notation) is given by the water input.

By combining Equations 17 and 18, one can solve the moisture balance equation at each layer. This solution is known to be in many cases a valid approximation to the solution of the Richards equation (see Supporting Information S1 for a comparative analysis of the solution to the compartmental model with that of HYDRUS-1D simulations (Šimůnek et al., 2012)).

Mass transport associated with water fluxes through the soil column is characterized accordingly. Equations 6 and 7 extends naturally Equation 1 to include a transport term T_A in the vertical direction, resembling 1D equations for reaction-diffusion processes hosted on a network support (Contemori et al., 2016; Nakao & Mikhailov, 2010). We consider the mean solute concentration C_A^i computed as $M_A^i / (n\, Z_r s^i)$, and assume that this mean concentration is transported along with water from one layer to the lower layers (well-mixed assumption). Although relaxable in lumped approaches by using a travel time formulation of transport (e.g., Benettin et al., 2021; Dagan, 1989; Rinaldo et al., 2015), this assumption seems a reasonable starting point when, owing to the layer depth, the mean flow advection is small compared to dispersion. In turn, this would imply relatively low average Péclet numbers ($Pe \ll 1$, even considering tension and moisture fluctuations), within each layer (Dagan, 1989; Fiori & Dagan, 1996). The transport term in Equation 1 can thus be expressed by:

$$T_A^i = \sum_{j \neq i} q^{i,j} C_A^j - C_A^i \sum_{j \neq i} q^{j,i} \tag{19}$$

which represents the net mass input of solute species A to soil layer i by mass transfer from/to other layers.

2.2.3. Computation of Time-Dependent Redox Potential E_h

In any redox reaction, the current resulting from the electron transfer process from electron donor to acceptor defined by the redox potential is induced by a voltage gradient that can be detected by an electrode immersed in aqueous solution (E_h). We define the generic redox reaction (composed of two half-reactions):

$$aA + cC \rightarrow bB + dD \tag{20}$$

For species at equilibrium, the relationship between the concentration and the E_h value is given by the adapted Nernst equation (Anderson, 2005; Zhang & Furman, 2021):

$$E_h = E_h^0 - \frac{RT}{n_e F} \ln \frac{[B]^b [D]^d}{[A]^a [C]^c} \tag{21}$$

where $[\cdot]$ is the activity of a given compound F is the Faraday constant and ne^- is the number of electrons exchanged in any single half-reaction defined as:

$$A + ne^- \Leftrightarrow B. \tag{22}$$

Equation 21 can be expressed in term of an intensive parameter pe defined by analogy to pH measurement of H^+ activity:

$$pe = \frac{F}{2.3RT}E_{eq} = -\ln\frac{1}{a_{e^-}} \tag{23}$$

When focusing on values of E_h of a single redox couple at constant temperature (as in our controlled experiments), modeling the net flow of electrons is equivalent to modeling the time evolution for the concentration of the two components of the redox couples. However, while these definitions hold for a single species, the relation between pe and E_h is less straightforward when multiple species are simultaneously involved. When E_h or pe are measured in aqueous solutions, the interpretation of the redox reading is problematic as several redox couples are involved and they are not all necessarily at equilibrium. Although the analytical expression for a generic case of m redox couples has been derived by Peiffer et al. (1992), the applicability of the exact solution remains limited even when only a few couples are involved due to the large number of parameters. However, if one redox couple is orders of magnitude out of equilibrium, it may overcompete all the others in terms of redox potential. Such a condition is generally assumed to be valid for the practical interpretation of redox measurements, allowing the approximation of the overall E_h as the sum of each single contribution.

To simulate the time evolution of E_h values, the following scheme is thus adopted: (a) the concentration of each redox couple is updated at each time-step based on the time integration of the transport and microbially mediated kinetic reaction Equation 1, and (b) a new E_h value is calculated for a generic redox reaction j by:

$$E_h = E_h^0 - \frac{RT}{F} \sum_j \frac{1}{ne_j^-} \ln\left[\frac{[B]^b[D]^d}{[A]^a[C]^c}\right] \tag{24}$$

where ne^- represents the number of electrons exchanged by each chemical reaction listed in Table 1. It is worth noting at this point that when a single metabolism is dominant, the dual behavior of a redox couple expressed by Equations 8 and 9 together with the Nernst equation defines weather a time scale separations between microbial and hydrologial process can arises. Indeed, by computing the time derivative of the Eh as follows:

$$\dot{E}_h \propto \left[\frac{RED_A - OX_A}{A} + \frac{RED_B - OX_B}{B}\right] \Rightarrow \dot{E}_h = \dot{E}_h(g(s), f(s)). \tag{25}$$

we observe that redox potential can be qualitatively described in terms of the only functions g and f, where the second relashonship holds for reaction rates spanning on time scale longer than the hydrological fluctuations. In the next section, we will illustrate how our designed experiments precisely Identified the edges of validity of this hypothesys, providing, thus, a solid reference for further interpretation of redox pattern.

3. Results

In this section we illustrate the comparison between measured and modeled responses of E_h to the imposed experimental conditions for the experiments SM-B, SM-I1 and SM-I2. The full list of parameters adopted in the model are reported in Table 2. Differences and similarities emerging among the three setups will be specifically addressed, in particular for (a) sharp fluctuations in soil saturation, and (b) smooth transitions.

3.1. E_h Evolution Under Sharp Fluctuations of Soil Saturation

The soil-moisture-blind experiment (SM-B, Figure 2) exhibits large changes in E_h values at all depths, except at the bottom layer (not shown) which was affected by air intrusion from the bottom drainage tube. Redox potentials reaching values below 100 mV were observed in the top two, organic-rich, layers at the onset of saturation conditions. A larger decrease in E_h values was observed in the mid-depth positions for saturated conditions only after 25 days. This is attributed to the abundance of bioavailable organic carbon. The low values reached in the top two layers at the end of each saturation cycle support the role of organic carbon (released from the top layer) in activating microbial metabolism and the associated consumption of dissolved oxygen. The variation in timing and intensity of the response at each depth is reflected in the increasing redox values observed during the drainage phase, which implies a defined vertical gradient of oxygen exposure during the free-drainage process.

The DOC concentration measured at the end of each saturated phase exhibits an initial vertical gradient (with higher values due to the leaves' presence) that slowly advances owing to the draining phase. The behavior of

Table 2
Summary of Model Parameters Used for Experiments

Symbol	Description	Units
Soil parameters		
$\tilde{K}_{sat}$	Effective hydraulic conductivity	[m/d]
n	Porosity	-
Z_r	Depth of layer	[cm]
s_{fc}	Soil field capacity	[-]
b	Soil-water retention exponent	[-]
s_{tr}	Soil moisture oxic transition threshold	[-]
β	High soil moisture limitation factor exponent	[-]
ζ	Low soil moisture limitation factor exponent	[-]
$\tilde{D}_s$	Oxygen diffusion coefficient	m^2/d
H_o	Oxygen Henry's coefficient	[-]
Reduction/Oxidation kinetic rate		
C_i	Concentration of the i specie	[mM]
E_h	Redox Potential	[mV]
ν_i	Stoichiometric coeff. Of the i specie	-
k_{RED,O_2}	Aerobic reduction rate	[kg^2/cell/g/d]
k_{RED,NO_3}	Total nitrate reduction rate	[kg^2/cell/g/d]
$k_{RED,Fe}$	Fe-reducers reduction rate	[kg^2/cell/g/d]
$k_{RED,S}$	S-reducers reduction rate	[kg^2/cell/g/d]
γ	DNRA/denitrification partition factor	[-]
K_{OX,NH_4}	Nitrification rate	[kg^2/cell/g/d]
$k_{OX,Fe}$	Fe-oxidation rate	[1/d]
$k_{OX,S}$	S-oxidation rate	[1/d]
BM	Conentration of biomass	[cell/kg]
r_A	Biomass growth rate	[cell/moles/d]
k_{BD}	Biomass decay rate	[1/d]
S_i	Soil release source of i specie for $i = DOC, Fe^{2+}$	[mM/d]
V_i	Inhibition factor of i specie	[moles/kg]

nitrate, ammonium and sulfate (see Figure S6 in Supporting Information S1) reflected the non-monotonic trend of E_h, suggesting the presence of an unexpected oxidizing region at the depth between 25 and 35 cm.

The transport parameters of the compartment model were chosen by imposing zero flux during the saturation periods at the bottom layer (i.e., no drainage) and by setting the effective saturated hydraulic conductivity K_{sat} to match the effluent flow integrated over the draining phase. The coefficients (k_{red} and k_{ox}) appearing in the reduction and oxidation rates in the compartmental model were calibrated against the experimental data by running a Bayesian (Markov Chain Monte Carlo) calibration using the DREAM$_{ZS}$ algorithm (see Table S1 in Supporting Information S1, reporting all parameter values adopted in the various and (Ter Braak & Vrugt, 2008; Vrugt et al., 2010) for details on Bayesian calibration). The simulated soil saturation dynamics for each layer, shown in Figure 2a, are consistent with the time shift of the oxidation phase observed at small depths (within the first 15 cm) in the E_h data (Figure 2b). We note, however, that the model systematically overestimates the reduction rate for the middle layer and it tends to over-predict the rising limb of the E_h curve for the two bottom layers (Figures 2c and 2d).

In contrast to SM-B, the depth-resolved, continuous monitoring of both redox potential and soil saturation in experiment SM-I1 enables the direct interrogation of the linkages between the two signals. Figures 3 and 4
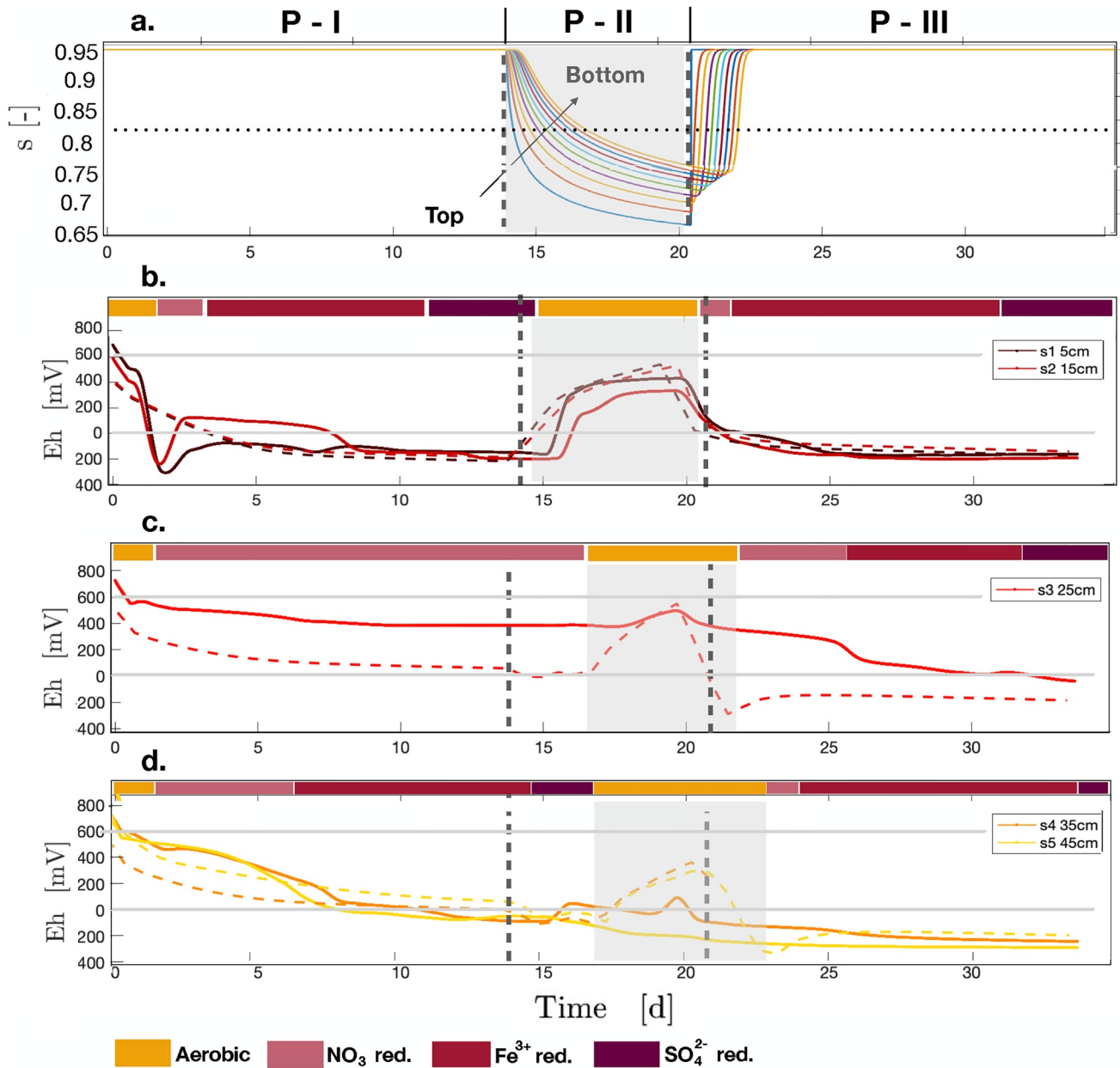
Figure 2. SM-B experiment. Top panel (a): simulated soil saturation dynamics for 10 layers. The phases are: I) saturated condition with water ponding and no flux at the bottom, II) free gravity drainage phase with subsequent water application regime, and III) second saturated regime with no flux at the bottom. The compartment layer predicts a slow desaturation that starts from the top layer (blue line) and then propagates downwards as indicated by the arrow. The horizontal black dotted line indicates the s_c value. From panel (b) to (d) the measured redox potential as a function of depth (solid line) compared with the output of the compartment model (dashed line) for the same depth. The gray shadows indicate the time windows during which the model predicts prevalently oxic conditions.

illustrate the time series of soil saturation at four depths, and E_h values at six depths, respectively. The relative homogeneity observed in soil moisture patterns across the lysimeter (i.e., across all layers) is to be attributed to the rapid drainage (suction pressure of -60 KPa applied at the bottom) and heavy precipitation events (3.5 L of rainwater applied in a few minutes). Such homogeneity is not reflected in the vertical heterogeneity of the E_h response in the phases post organic carbon amendment. During the first three cycles (C-I, C-II, and C-III) corresponding to no organic carbon amendment, experiment SM-I1 shows a limited decrease in redox potential during the saturation period with a maximum decrease in the redox potential of $\sim$226 mV and a minimum E_h value of $\sim$189 mV. The value is referred to as a silver chloride electrode as a reference electrode, thus each value must be positively shifted by 205 mV around, considering a room temperature of 25°. After accounting for the
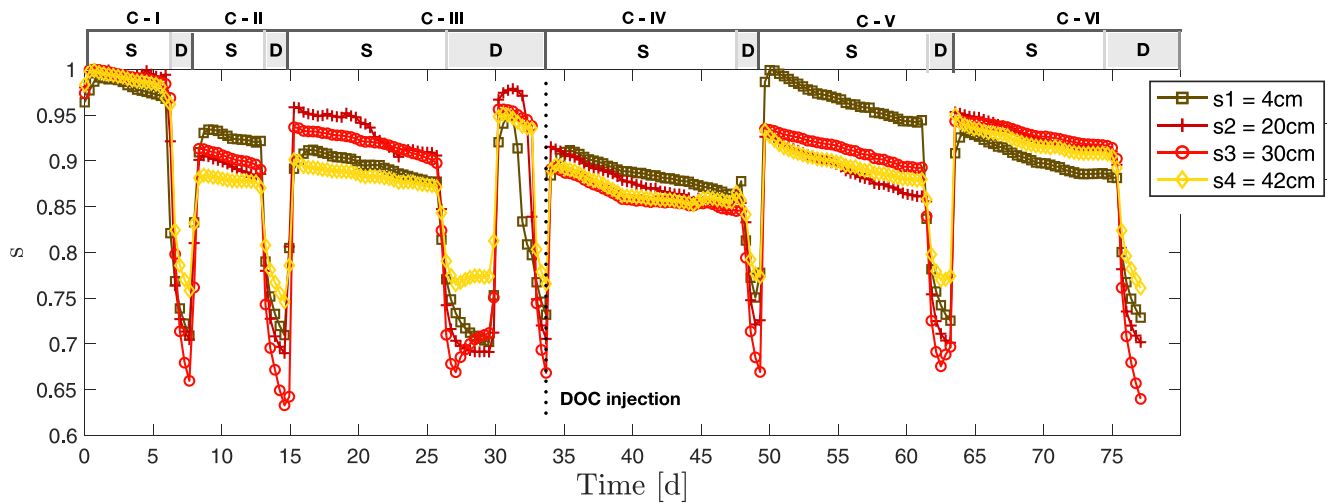
Figure 3. SM-I1 experiment: measured soil saturation time series at four different depths from top layer (darker) to bottom layer (lighter color). During the saturated phases (S), closed boundary conditions (no flow) were held. The unsaturated (drainage, D) phases were induced by a vacuum pressure applied at the bottom valve (see Supporting Information S1 for details). Saturation/drainage cycle numbers as indicated by C-I, C-II, etc. Carbon amendment is indicated by a dashed vertical line.

reference electrode shift, the range of values of the redox ladder associated to each metabolism falls in the regions represented in Figure 1c. The subsequent three cycles (C-IV, C-V, and C-VI) received organic carbon amendment. Negative E_h values were observed in these cycles but only at the top and the bottom of the soil column. This spatial heterogeneity may be attributed to a varying availability of organic carbon supply, possibly coming from potential air entrapment in the middle of the lysimeter. This mechanism could inhibit the establishment of reducing conditions. Conversely, the negative drop of redox potentials experienced by the bottom layer (around day 40) and the top layer (around day 50), would seem to indicate the timing of the activation of the other two alternative metabolisms: ferric and sulfate reduction. This interpretation is supported by the following evidence.

In Figure 5, the concentration of nitrate decreases during cycles C-I, C-II, and C-III (during the first 40 days), while ferrous iron and sulfide concentrations are close to the detection limit, suggesting that nitrogen reduction is the dominant metabolism. After carbon amendment in cycle C-IV, nitrate was consumed rapidly, and the reduction of Fe(III) and sulfate (the latter to a lesser extent) proceeded, in agreement with the order of the TEAP. The model reproduces the measured concentrations reasonably well. We observe that while the frequency of the pore-water sampling was insufficient to characterize the concentration trends of the three compounds in detail,
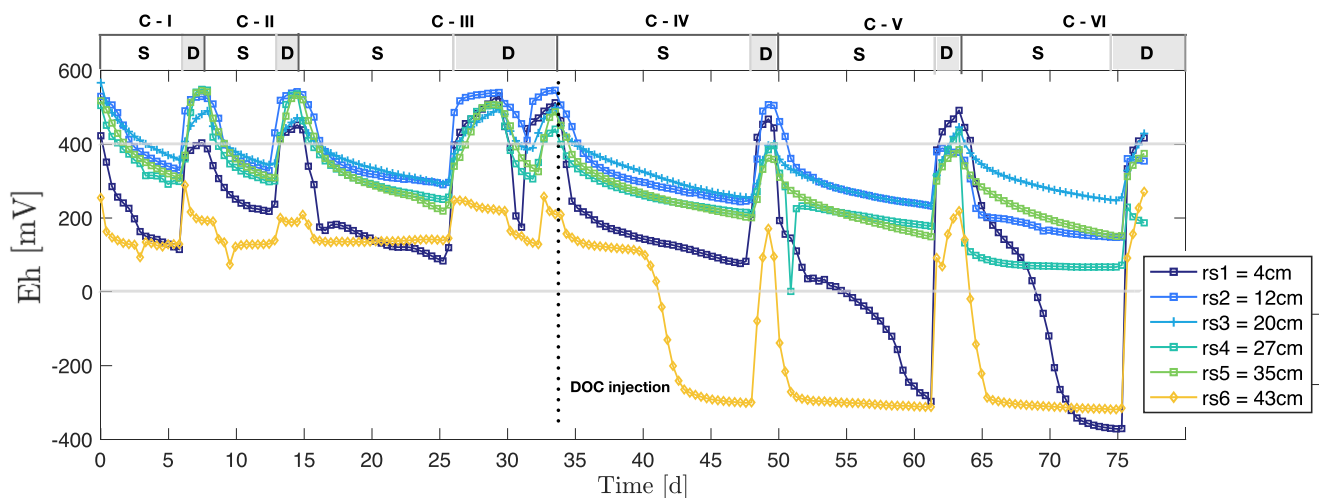

Figure 4. SM-I1 experiment: measured redox potential time series $E_h(t)$. All the layers share common behavior before the carbon addition at 34 days, suggesting that aerobic respiration and nitrate reduction are the major metabolisms underway. After carbon addition, the bottom layer and, subsequently, the top layer reach lower E_h values compatible with iron and sulfate reduction (the latter triggered in the redox range of −200 to −550 mV (e.g., Rodríguez-Escales et al., 2020)).
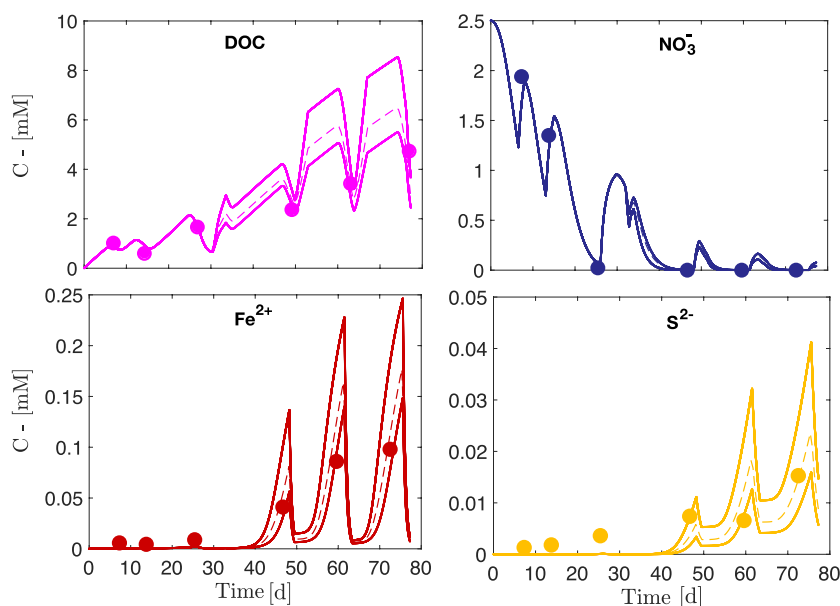
Figure 5. Concentration of dissolved organic carbon, NO_3^-, Fe^{2+} and S^{2-} for SM-I1. Samples (dots) were collected during each draining phase (see Supporting Information S1 for details). Simulations from the compartment models are shown through lines that indicate the mean (dashed) and standard deviation (solid) among all the layers. The decrease in nitrate followed by the increase in iron and sulfide is consistent with the hierarchy of electron acceptors.

the model predicts a highly oscillating behavior of the system. We suggest that this effect is not an artifact of the model, because the same trend had been experimentally reported elsewhere (Ginn et al., 2017), where pore-water chemicals were sampled at higher frequency.

The clear synchronization between soil saturation levels and the corresponding E_h values in the middle layers highlights how fluctuations of the former strongly drive the dynamics of the latter. Figure 6 illustrates the agreement between data and simulations of the full biogeochemical model (Section 2.2.2) by comparing the time derivative of the measured redox potential versus the one numerically computed. This result was not surprising as the timing of the peaks in E_h concurred with the sharp changes in soil moisture, supporting the interpretation of Equation 25, where redox transitions could be analytically described by ad-hoc calibration of the functions $f(s)$ and $g(s)$ only by simply summing the two functions modulated by a fitted amplitudes factor. Our computational scheme, supplied by measured soil saturation, reproduces well the redox potential fluctuations in particular for the middle layers (Figure 6). However, when the model is applied to the bottom and top layers (Figure 7), discrepancies arise during the transition from nitrate to iron reduction. A reason for this discrepancy may be found in the impact of local heterogeneity on the relevant transport processes. Small-scale spatial heterogeneity in the
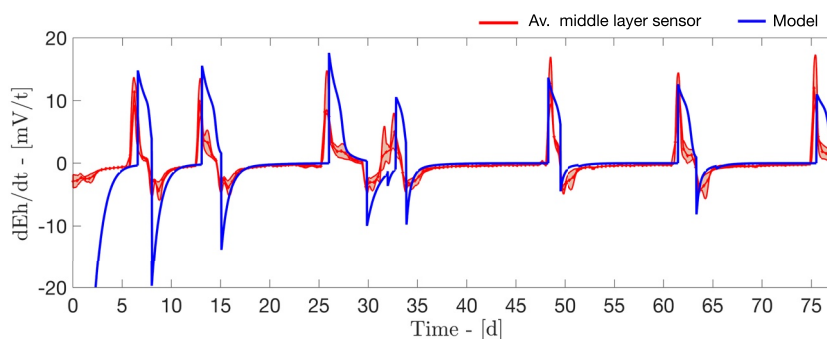

Figure 6. Time derivative of the SM-I1 redox potential for the middle layers (depth 12–35 cm). Measurements are indicated in red (mean and standard deviation across the different sensors) and model simulations in blue. Simulations are based on Equation (25).
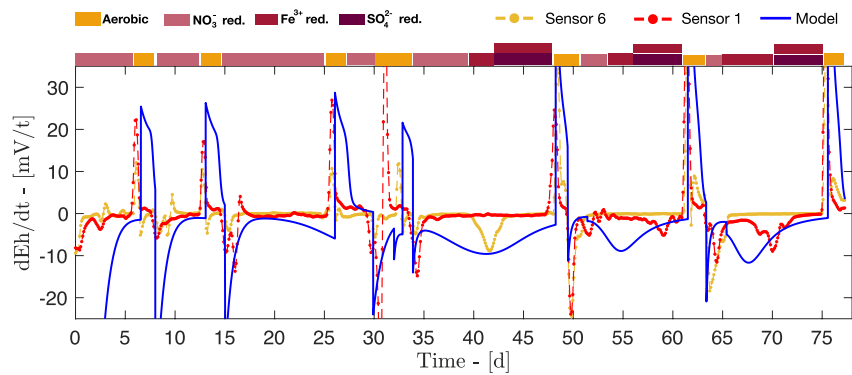
Figure 7. Time derivative of the SM-I1 redox potential for layer 6 (dashed yellow line) and layer 1 (dashed red line) against model predictions (solid blue line). Similar to Figure 2, the time window of the predominant metabolism simulated by our model is indicated on the top by the color bars. The first three cycles are dominated by aerobic respiration and nitrate reduction while from at half of the fourth cycle (after 45 days) the downward peaks indicate transition from nitrate to iron and sulfate reduction (the latters occurring simultaneously although with different relative contributions described by the limiting function Θ).

air-water distribution, porosity, hydraulic conductivity and, possibly, the presence of preferential flowpaths is expected in any natural soil, but it was not evident in our few moisture sensors, precluding the accurate prediction of E_h transitions. Further, no depth-resolved pore-water sampling was performed due to the absence of suction cups. Thus, pore-water composition was only obtained as an integrated value for the entire lysimeter upon drainage (over 24 hr). Lack of information about the vertical gradients therefore prevented the probing of the hypotheses concerning heterogeneous DOC and BM spatial distributions. In particular, the evidence that similar soil saturation values would arise almost at the same time at all depths, combined with the fact that DOC was dissolved in the applied inputs, suggests that the downward flux of DOC is actually distributed in a complex manner, perhaps engaging preferential flowpaths, during saturation phases.

While internal fluxes and preferential flow paths prove relevant to describe the slow decreasing trend of the redox potential for different depths, we will show in the next section that the prediction of spikes in the E_h signal requires in general a careful analysis and a deeper comparison between E_h and soil saturation data, ultimately suggesting a redefinition of the condition for oxic/anoxic transition expressed by Equations 4, 5, and 25.

3.2. E_h Evolution Under Smooth Soil Moisture Transitions

The fluctuating hydrologic regime chosen for experiment SM-I1 highlights the importance of the modulating functions, $g(s)$ and $f(s)$, especially in identifying the critical value s_{tr} that defines the onset of the transition between oxic and anoxic conditions. Such value had been assumed to be the soil field capacity s_c (Calabrese & Porporato, 2019; Manzoni & Porporato, 2007). When compared to soil saturation data, our observed patterns of redox potential agree with the interpretation of the pivotal role of $f(s)$ and $g(s)$. If this were generally true, the identification of the critical value s_{tr} found in the SM-I1 experiment should be sufficient to track the soil moisture signals measured in SM-I2 because they share the same soil type and experimental set-up.

Because in the experiment SM-I2 the soil was maintained under saturated conditions above the critical value $s_c = 0.85$ for extended periods of time, the second condition imposed in system (4) and (5) for g and f was always satisfied. Thus, E_h fluctuations were expected to be fully controlled by the moisture behavior. However, when comparing the soil saturation signal of the top three layers (Figure 8c.) with the E_h responses at the same depths (Figure 9a.), it is clear that this is not the case. Data at all depths exhibits both rapid and slow fluctuations. The former are due to daily irrigation-drainage regimes, whereas the latter are mostly driven by nonlinear responses of soil saturation to wetting/drying cycles and by the related hysteretic effects (e.g., Hornberger et al., 2014). Although both types of fluctuations share the same range of amplitudes (meaning that the saturation level decreases down to similar values), not all of them have a direct counterpart in the measured redox signals. Thus, our experiments suggest that a key factor in defining oxic/anoxic transitions is how rapidly these fluctuations occur—rather than their intensity.
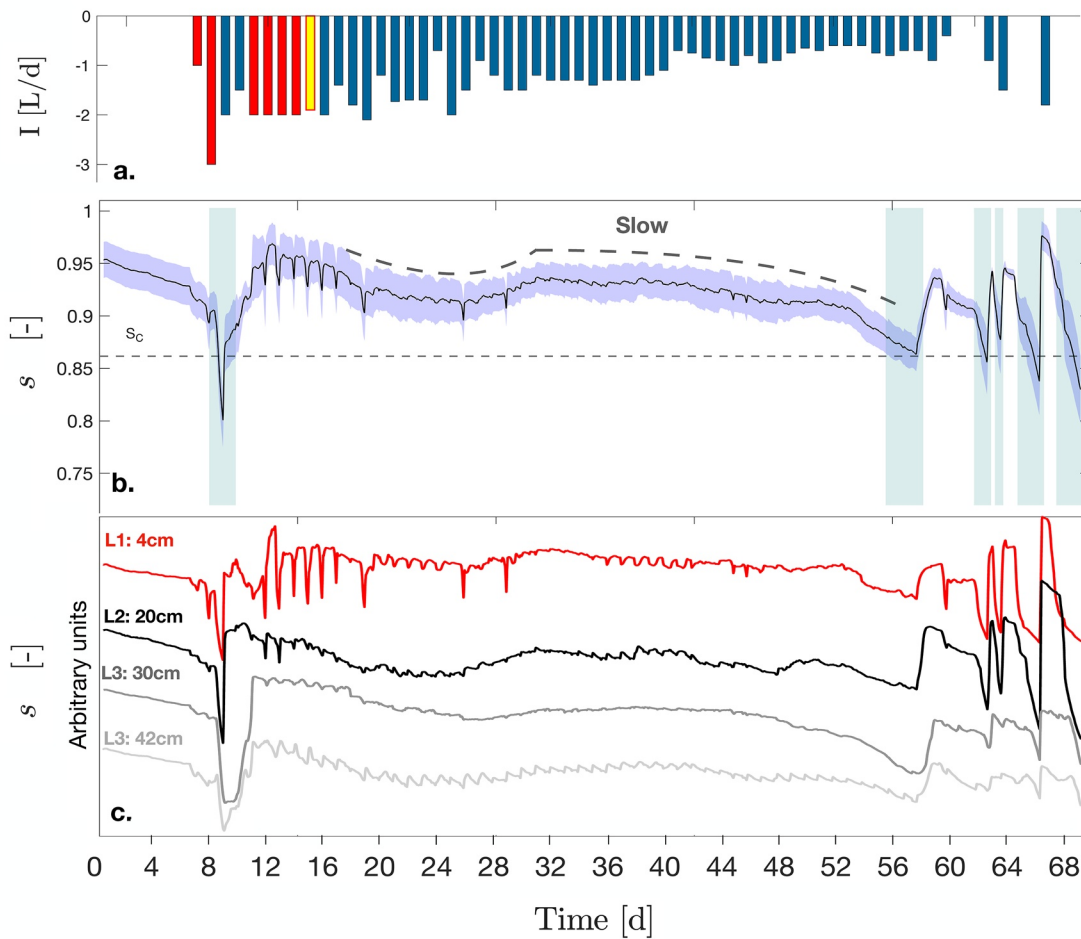
Figure 8. Hydrological regime for SM-I2. (a): Water application schedule. The bars' size indicates the daily irrigation amount, while the colors refer to distinct rainwater solutions: in blue normal rainwater, red for rainwater with dissolved organic carbon (DOC) and yellow for rainwater with DOC and nitrate. (b): Mean and standard deviation of measured saturation data across the four depths. Light green regions indicate the selected time window during which a single value for s_{tr} was imposed for layers 1,2 and 3, corresponding to rapid oxic transitions. (c): The soil saturation signal at each measured depth. The signals are arbitrarily shifted to better distinguish them. The top layer dynamics are more sensitive to the irrigation and bottom suction patterns than deeper layers (see especially days 12–32).

Figure 9a highlights (gray shaded areas) the time windows that correspond to oxic transition in experiment SM-I2 as measured by redox sensors 2 and 3. These transitions are well synchronized with saturation fluctuations at the same depth (panel c) but they are not correlated to their magnitude. Thus, any unique threshold value in the soil saturation value will evidently fail to catch the full spectrum of transitions. Instead, Figure 9b illustrates how the timing of the redox potential peaks corresponds almost perfectly with the time derivatives of soil saturation above a critical value. Thus, by selecting the time windows according to this criterion, the model correctly predicts the timing of the redox potential transitions once the condition in system (4) and (5) is imposed to the time derivative of the moisture rather than its absolute value itself. The corresponding $g(s)$ and $f(s)$ time series are then obtained by filtering in time when $\dot{s}(t)$ is above a suitable threshold ($\sim 0.01 [d^{-1}]$ in this work).

Our experimental evidence provides an accurate definition of "rapid change" for redox potentials and highlights the inadequacy of relying on a single critical threshold value for soil moisture (say, the parameter s_c) to provide a reliable predictor of the actual oxic/anoxic transitions when they are moderate in intensity but frequent in time. Therefore, to predict redox spikes in experiment SM-I2, the analysis of moisture cycles based on a single threshold value of soil saturation fails to determine whether or not the system shifts from anoxic to oxic conditions from a redox potential perspective. We conclude that the analysis must include an examination of the time derivative of the soil saturation signal. From a microbial perspective, this is tantamount to considering whether any external soil moisture perturbation lasts longer than the (inverse of the) relevant oxygen consumption rate. Once the
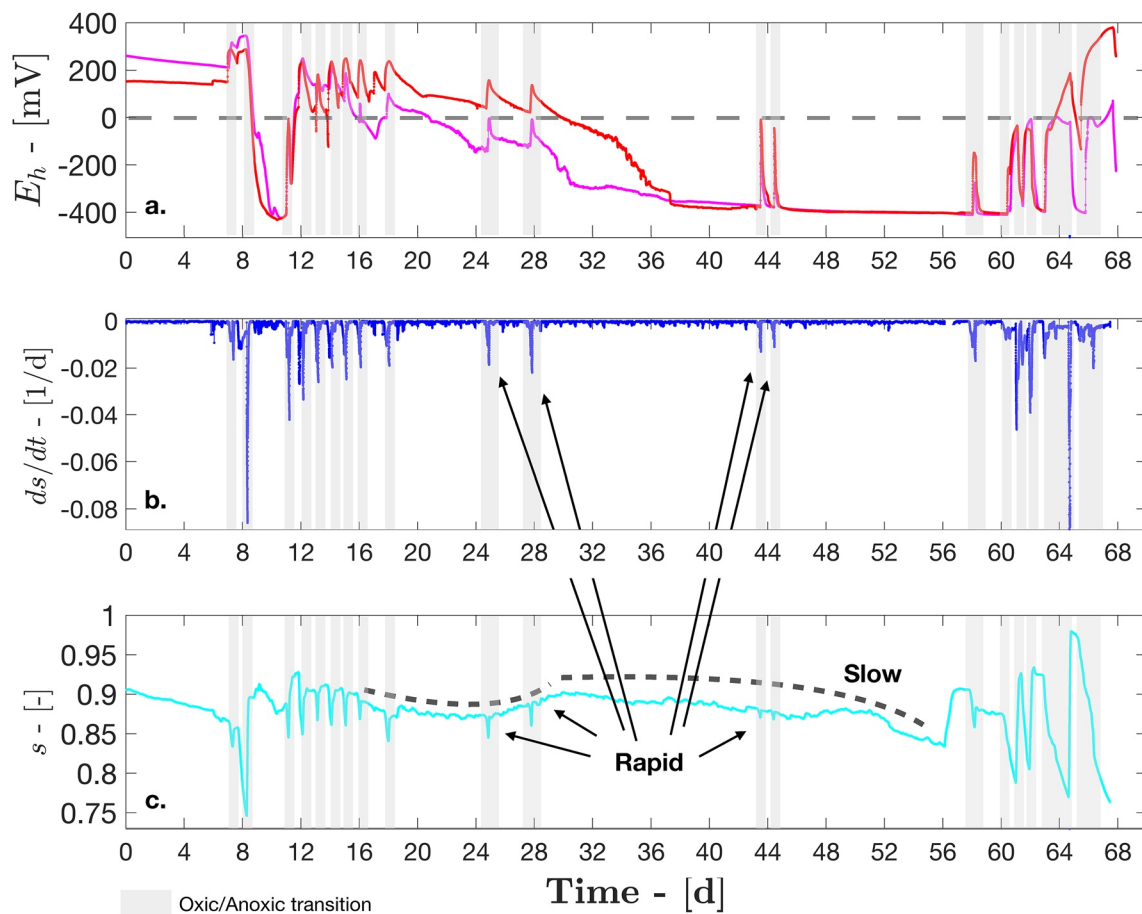
Figure 9. Predicted and measured anoxic/oxic transitions for SM-I2. (a) Redox time series for sensors 2 (red) and 3 (magenta) both placed in the depth range between moisture sensors 1 and 2. The gray shadows correspond to rising redox potential phases. (b) Time derivative of the mean of saturation measured by sensor 1 and 2. Only peaks above a threshold value are significant to describe the timing of the anoxic/oxic transitions. (c) The mean of saturation level measured by sensors 1 and 2.

previous analysis of the time series of saturation is extended to the other soil moisture sensors we can feed the compartment model with a more realistic depth resolved time series of $g(s)$ and $f(s)$.

Figures 10a–10c show the time series of the redox potentials measured in the experiment SMI-2 for the first, the middle and the bottom layers respectively. The top layer exhibits the highest fluctuations between 6 and 17 days. This is due, in large part, to the abundance of DOC in applied water, leading to sufficiently rapid microbial growth to deplete oxygen and nitrate and allow iron and sulfate reduction to occur and to respond almost instantaneously to daily moisture content cycles and influx of oxygenated and DOC-rich water. When organic carbon amendment was halted (from day 15), DOC was flushed out from the top layer by advection resulting in decreased microbial activity and in decreased consumption rate of oxygen coupled to the daily supply from oxic applied water. Such downward flux of DOC was responsible for the decrease in redox potential in the lower layers that smoothly shifted to alternative metabolisms as shown in Figures 10b–10c. As already found in the previous two experiments, a counterintuitive trend in the E_h response is reported for middle layers (sensor 5, precisely). Whether this behavior can be attributed to either the hydrological drivers or a different microbial response will be discussed in the next section.

4. Discussion

The comparison between the model prediction and the experimental data in SM-B, evidence a relevant inconsistency in the mid layers positions, where the redox potential behavior seems to be delayed when compared to both top and bottom layers. This could potentially be attributed to both the abundance of bioavailable organic carbon or to an adaptation of the microbial community. However, the vertical gradient on the measured concentration of
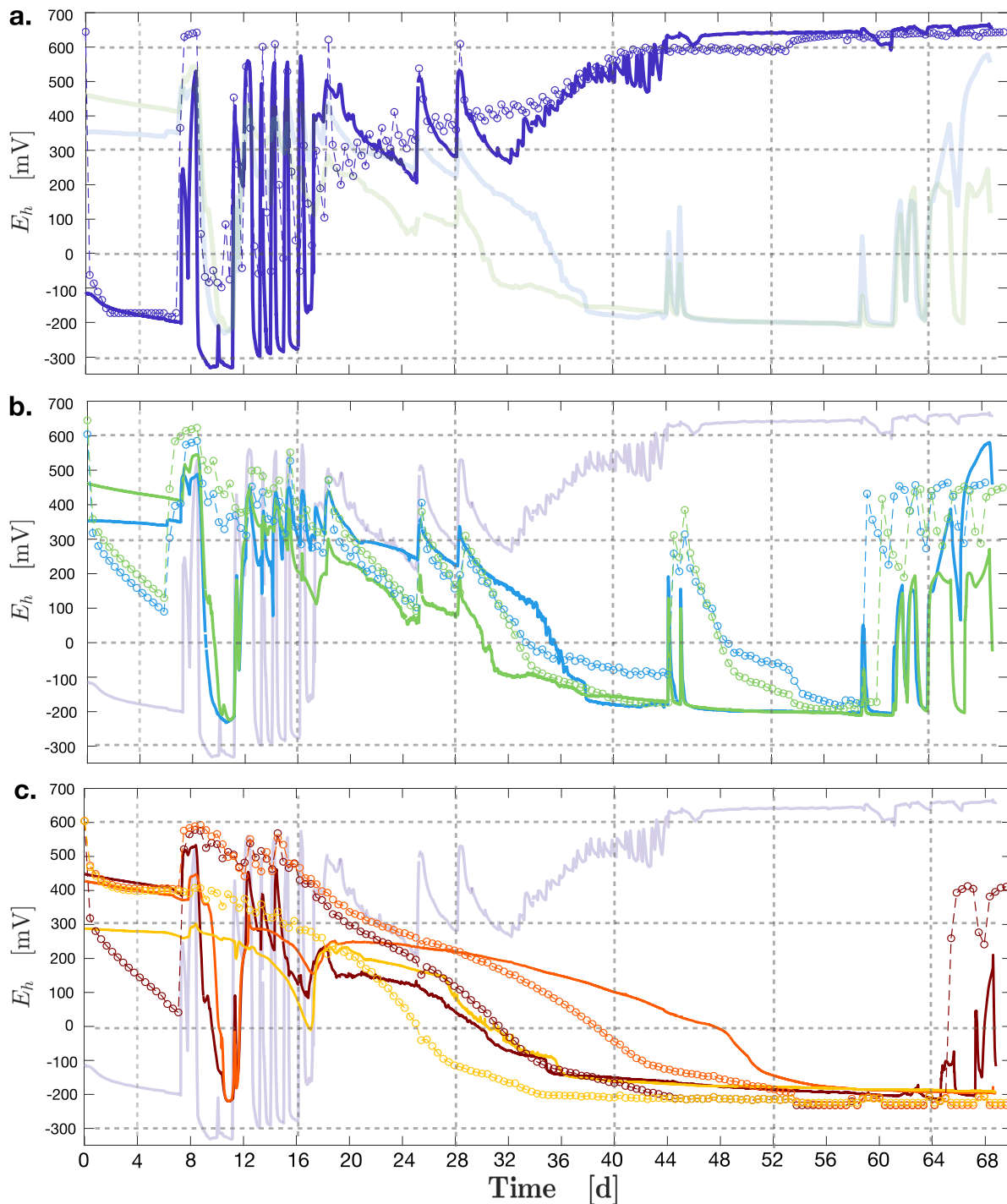
Figure 10. Redox time series for experiment SMI-2. (a) The top layer. Sensor data (blue solid line) versus model prediction (circles). The model is able to reproduce the relevant peaks of the initial phase and the rising positive trend later in the time series. In transparent light green and light blue lines: redox data from sensors 2 and 3, respectively; (b) Redox time series for experiment SMI-2, for sensors 2 (green) and 3 (sky blue). Sensor data are in solid lines while the model is in circles/dashed line. The model is able to reproduce the relevant trends in both layers. The model tends to underestimate the decrease observed in the first week. We interpret this decrease as resulting from the transport of dissolved organic carbon (DOC) to lower layers. In light purple, data of sensor 1 are reported as a reference to highlight the opposite trend starting at 32 days of continuous water application; (c) Redox time series for experiment SM-I2, for sensors 4 (brown), 5 (orange), and 6 (yellow). Sensor data are in solid lines while the model is in circles/dashed lines. The top layer is plotted in light purple for reference. The initial decrease in redox potential is interpreted as resulting from the transport of DOC to lower layers through preferential flow paths, a process which is underestimated by the compartment model.

DOC as shown in Figure S4a in Supporting Information S1 suggests that the former provides a more convincing explanation.

We further highlight the role of the hydrological drivers by showing the results of the chemical analysis in Figure S6 in Supporting Information S1. The concentrations of sulfate, ammonium and iron II suggest the coexistence of both oxic and anoxic conditions. A reasonable explanation for the persistence of high E_h values at mid-depths may invoke the presence of residual oxygen in air-filled pores due to air trapping. Another explanation could be the limited supply of DOC, precluding nitrate consumption. This explanation, if confirmed by direct experimental evidence, would underpin the importance of depth-resolved soil saturation data.

The controlled feeding solution in the irrigation water for experiment SM-I1 provides direct evidence of the role of the native organic carbon and its release rate S_{DOC} as shown in the first three cycles of both Figures 4 and 5. In the absence of DOC amendments (cycles C-I, C-II, and C-III), the redox cycles respond to moisture addition but the redox potential does not drop below +150 mV.

The imposed rapid drainage phases driven by high suction imply an equally rapid intrusion of oxygen at all depths. This is particularly evident for the middle layers (12–35 cm depth) where the redox measurements span a similar range of values which correspond to aerobic respiration and nitrate reduction. As both oxygen and DOC are supplied from the top, we could argue that the system reached its quasi-steady state at the end of each saturation phase (meaning that the DOC available is enough to consume both all oxygen and nitrate available), otherwise a vertical gradient from top to bottom would have been expected. Under these conditions, the functions $f(s)$ and $g(s)$ are expected to adequately describe the redox potential dynamics.

The hydrological regime chosen in SM-I1 case imposed a clear separation between saturated and unsaturated phases as shown in Figure 3. This implies that the functions $g(s)$ and $f(s)$ well describe the oxidation and reduction transitions that happen in a somewhat binary manner, that is, on/off, rather than underpinning smoother transitions (see Equation 25). Indeed, as noted before, sharp transitions in saturation levels are promptly reflected in the redox transitions. However, a formulation using the $f(s)$ and $g(s)$ functions alone cannot address –by design– the full dynamics of the competition between the various electron acceptors within a given soil saturation condition. This can be achieved through the use of the limiting factor Θ_A. As shown by a quick comparison between Figures 6 and 7 where the series of negative drops at the day 40, 55, and 67 associated to the switch between ferrous to sulfide reduction cannot be explained by saturation state variable's function only. However, even with this addition, the exact timing of the decreasing limbs during the prolonged anoxic phases for layers 1 and 6 (when the system switches from nitrate to ferrous consumption) is hard to predict. The rapid drainage/wetting transitions likely enhance the formation of preferential flow paths and pose the problem of evaluating the degree of mixing at any depth. These effects are mitigated in case of smoother soil moisture fluctuations and more constant internal fluxes. This is precisely the case for the hydrological regime chosen in the experiment SM-I2. As shown in Figure 8b, all four sensors lie in a narrow saturation range of 0.95–0.99 for most of the time. Note that the experiment was conducted in highly saturated condition close to Darcy regimes (Dagan, 1989) for most of the time, with the following consequences: (a) it is reasonable to neglect hysteretic effects otherwise accessible only via soil water retention curve calibrations, and (b) internal fluxes may be assumed to be continuous and smoother than in experiment SM-I1. Here, by comparison between the results of the compartment model and the E_h sensor data (shown for the first, the middle and the bottom layers in Figures 10a–10c, respectively), we conclude that the model captures E_h variations reasonably well for each layer. This highlights the crucial role of the functions $g(s)$ and $f(s)$ in determining the oxic-anoxic transition and in capturing the main trends observed at all depths.

As DOC is the main fuel for microbial activity, the discrepancy between the general data trend and the output of the model, especially at sensor 5, calls for an explanation (Figure 10c). The model for E_h for this layer exhibits a delayed decrease to more negative values (relative to the measured data), which is different from the behavior of sensor 4 and 6 and cannot be explained by the nitrate breakthrough curve. If this had been the case, the temporal delay would have been consistent with the spatial shift in sequential order, which does not appear from the data. This anomalous trend was recurrent in all the three experiments (SM-B, SM-I1, and SM-I2). Our interpretation is that the measured trend could be attributed to transport process, likely induced by a combination of preferential flow paths and gas entrapment. In fact, the former would enhance more rapid carbon supply at the lower layers, while the latter could partially inhibit anaerobic metabolism due to the possible persistence of air bubbles. Thus, a different partition of the downward flux, expressed by the related terms $q_{k,i}$ in Equation 16, would suffice in

providing an effective mechanism capturing the inverse trend of vertical redox signals (see the Supporting Information S1 for the related matrix flux coefficients). At present, however, an estimation of the off-diagonal terms of the flux matrix remains qualitative and thus speculative. The reason lies in the number of free parameters that the flux matrix may admit, that is, the possible connections between layers and their partitioning coefficients, making plausible a prediction of the anomalous behavior of middle layer by non-unique sets of combinations of the redistribution of fluxes between top to bottom layers. A rigorous quantification of the hydrological features and a proper calibration of all the terms $q_{k,i}$ and $q_{i,k}$ of the network fluxes of the compartmental model could possibly be tackled by monitoring the transport behavior by a reasoned use of experiments using passive tracers dissolved in the water application. Its characterization (say, in the form of measured breakthrough curves at suitable compliance surfaces, here identified as the various layers of the compartmental model) would resolve the definition of the actual flowpaths. On this issue further experimentation is ongoing.

Finally, while the model is able to capture the timing of each spike labeled in Figure 9 (gray shadow), the descending limb of the modeled signal is slower than that of the measured signal. This highlights, interestingly, the model's inadequacy in accounting for the consumption of both DOC and electron acceptor as well as the relative growth rate under the experimental conditions analyzed. A possible way to overcome this drawback might require to further develop the capabilities of the model to account for process-specific growth rates (e.g., Huang et al., 2021), including adaptation of competition where the reduction and oxidation rate constants are promoted to time/microbial population dependent function.

Obviously, our modeling approach is not devoid of assumptions that may be relaxed in future work. The assumption of a one-dimensional spatial description of the relevant transport processes is certainly a potentially gross approximation when soil microbial activity consequences are studied. However, this study shows that 1-D redox scenarios are interesting and highly nontrivial. The validity of the experimental patterns and simulation that we have observed are probably limited to fluctuating capillary fringes or to vadose zone setups. We do not deny the relevance of the insights that may be needed to understand many other contexts where 3-D representations may be needed where redox cycling may be driven by processes other than sub-vertical ones. In our view, however, a sensible way of proceeding is hierarchical, moving from the simplest (yet realistic) geometrical setting, the 1-D setup, to tackle in an orderly manner the considerable challenges already posed by the simple controlled environment of the experimental design. Moreover, it is likely that the long-term goal of our work, the response of natural soils to shifting patterns of precipitation, will mostly involve sub-vertical processes of the type studied herein. We argue that understanding redox potential cycling for a well-defined 1D system is relevant and representative of a large share of vadose zones.

The same considerations apply to the assumptions underlying our specific mass balances describing biogeochemical and hydrologic processes of interest. Although the compartmental models used here considerably simplify the flow and transport dynamics, they still do a satisfactory job in capturing the essentials of the experimental data. Moreover, when computed hydrological states are compared with the results obtained by full-fledged nonlinear models requiring a realm of additional information (SI), the comparison proves satisfactory allowing us to exploit the direct comparability of experiments and computations and a computational burden supporting Bayesian analyses. We thus claim that our conclusions are justified.

5. Conclusions

The following conclusions are worth mentioning:

- A synoptic view of coupled depth-time measurements of redox potential E_h, soil saturation and aqueous composition sheds light on the key drivers of the metabolic shifts of soil microbial communities. We have provided one such view by investigating the interplay between soil saturation dynamics and the corresponding E_h values in depth-time within a 50 cm soil column within a variously instrumented lysimeter settings under controlled conditions. We have quantitatively characterized the type of correlations (or lack thereof) emerging between soil saturation and E_h values via the resulting soil measurements under various imposed application and drainage conditions;
- Our main results deal with the experimental and computational determination of the highly nontrivial correlation between the dynamics of soil saturation and redox potential, the driver of change in soil microbial community composition. Spatially explicit mathematical models of reactive transport help interpret the

experimental data and define the relevant controls. We find experimental evidence that the velocity of the imposed change to soil saturation, epitomized by the time derivative of the saturation signal, discriminates the kind of rapid shift of redox potential that is thought to prompt oxic/anoxic transitions—and thus arguably the adaptations demanded by the soil bacterial communities. Overall, we succeed in reproducing in depth/time both the general trends and local spikes observed in the measured redox potentials;

- Our experimental results also highlight the importance of a proper characterization of organic matter availability and transport and of addressing to what extent rapid soil saturation perturbations may impact biogeochemical redox processes. We address the minimum amount of biogeochemistry needed to charatarize the dynamics of electron donors/acceptors that are ultimately responsible for the patterns of E_h not directly explained by physical oxic/anoxic transitions;

- The richness of measured patterns of the redox potential in depth-time shown by our experiments suggests a certain degree of prudence in interpreting bulk-averaged relations between soil saturation and redox conditions (say, averaging soil saturation and redox potentials across the root zone of vegetated soils). Artifacts of the assumptions would appear, in particular, when the spatial extent of the soil layer affected by redox cycles is likely to be significantly smaller than the averaging depth. This is the case in the particular hydrologic setups investigated in this work.

Forthcoming work will concentrate on the use of the information gained on the cycles of redox potential to design and execute experiments on soil bacterial community compositions under controlled hydrologic forcings.

Data Availability Statement

All data presented in this paper are openly accessible in Miele et al. (2022), under Creative Commons Attribution (CC BY) license.

References

Aller, J., Allecfr, R., Kemp, P., Chistoserdov, A., & Madrid, V. M. (2010). Fluidized muds: A novel setting for the generation of biosphere diversity through geologic time. *Geobiology*, *8*(3), 169–178. https://doi.org/10.1111/j.1472-4669.2010.00234.x

Anderson, G. M. (2005). *Thermodynamics of natural systems* (2nd ed.). Cambridge University Press. (OCLC: 61504712).

Benettin, P., Nehemy, M., Asadollahi, M., Pratt, D., Bensimon, M., McDonnell, J., & Rinaldo, A. (2021). Tracing and closing the water balance in a vegetated lysimeter. *Water Resources Research*, *57*(4), e2020WR029049. https://doi.org/10.1029/2020wr029049

Bickel, S., & Or, D. (2021). The chosen few—Variations in common and rare soil bacteria across biomes. *The ISME Journal*, *15*(11), 3315–3325. https://doi.org/10.1038/s41396-021-00981-3

Borer, B., & Or, D. (2021). Spatiotemporal metabolic modeling of bacterial life in complex habitats. *Current Opinion in Biotechnology*, *67*, 65–71. https://doi.org/10.1016/j.copbio.2021.01.004

Borer, B., Tecon, R., & Or, D. (2018). Spatial organization of bacterial populations in response to oxygen and carbon counter-gradients in pore networks. *Nature Communications*, *9*, 1–11. https://doi.org/10.1038/s41467-018-03187-y

Brun, A., & Engesgaard, P. (2002). Modelling of transport and biogeochemical processes in pollution plumes: Literature review and model development. *Journal of Hydrology*, *256*(3–4), 211–227. https://doi.org/10.1016/S0022-1694(01)00547-9

Calabrese, S., & Porporato, A. (2019). Impact of ecohydrological fluctuations on iron-redox cycling. *Soil Biology and Biochemistry*, *133*, 188–195. https://doi.org/10.1016/j.soilbio.2019.03.013

Contemori, S., Di Patti, F., Fanelli, D., & Miele, F. (2016). Multiple-scale theory of topology-driven patterns on directed networks. *Physical Review*, *93*(3), 032317. https://doi.org/10.1103/PhysRevE.93.032317

Dagan, G. (1989). *Flow and transport in porous formation*s. Springer-Verlag.

Daniels, W. L. (2016). Review of the nature and properties of soils. In R. R. Weil & N. C. Brady (Eds.), *Soil science society of America journal* (15th ed.). https://doi.org/10.2136/sssaj2016.0005br

Ebrahimi, A., & Or, D. (2015). Hydration and diffusion processes shape microbial community organization and function in model soil aggregates. *Water Resources Research*, *51*(12), 9804–9827. https://doi.org/10.1002/2015wr017565

Evans, C., & Findley, G. (1999). A new transformation for the Lotka-Volterra problem. *The Journal of Mathematical Chemistry*, *25*(1), 105–110. https://doi.org/10.1023/a:1019172114300

Falkowski, P., Fenchek, T., & Delong, E. (2008). The microbial engines that drive Earth's biogeochemical cycles. *Science*, *320*(5879), 1034–1039. https://doi.org/10.1126/science.1153213

Federle, T. W., Dobbins, D. C., Thornton-Manning, J. R., & Jones, D. D. (1986). Microbial biomass, activity, and community structure in subsurface soils. *Ground Water*, *24*(3), 365–374. https://doi.org/10.1111/j.1745-6584.1986.tb01013.x

Fiori, A., & Dagan, G. (1996). Finite peclet extensions of Dagan's solutions to transport in anisotropic heterogeneous formations. *Water Resources Research*, *32*(1), 193–198. https://doi.org/10.1029/95wr02768

Gibbons, S., & Gilbert, J. (2015). Microbial diversity-exploration of natural ecosystems and microbiomes. *Current Opinion in Genetics & Development*, *35*, 66–72. https://doi.org/10.1016/j.gde.2015.10.003

Ginn, B., Meile, C., Wilmoth, J., Tang, Y., & Thompson, A. (2017). Rapid iron reduction rates are stimulated by high-amplitude redox fluctuations in a tropical forest soil. *Environmental Science & Technology*, *51*(6), 3250–3259. https://doi.org/10.1021/acs.est.6b05709

Groh, J., Vanderborght, J., Pütz, T., & Vereecken, H. (2016). How to control the lysimeter bottom boundary to investigate the effect of climate change on soil processes? *Vadose Zone Journal*, *15*(7), 1–15. https://doi.org/10.2136/vzj2015.08.0113

Gubler, A., Wächter, D., Schwab, P., Müller, M., & Keller, A. (2019). Twenty-five years of observations of soil organic carbon in Swiss croplands showing stability overall but with some divergent trends. *Environmental Monitoring and Assessment*, *191*(5), 277. https://doi.org/10.1007/s10661-019-7435-y

Guillaume, T., Makowski, D., Libohova, Z., Elfouki, S., Fontana, M., Leifeld, J., et al. (2022). Carbon storage in agricultural topsoils and subsoils is promoted by including temporary grasslands into the crop rotation. *Geoderma*, *422*, 115937. https://doi.org/10.1016/j.geoderma.2022.115937

Hall, S. J., McDowell, W. H., & Silver, W. L. (2013). When wet gets wetter: Decoupling of moisture, redox biogeochemistry, and greenhouse gas fluxes in a humid tropical forest soil. *Ecosystems*, *16*(4), 576–589. https://doi.org/10.1007/s10021-012-9631-2

Hazen, T. C., Jiménez, L., López de Victoria, G., & Fliermans, C. B. (1991). Comparison of bacteria from deep subsurface sediment and adjacent groundwater. *Microbial Ecology*, *22*(1), 293–304. https://doi.org/10.1007/BF02540231

Hornberger, G., Wiberg, P., Raffensperger, J., & D'Odorico, P. (2014). *Elements of physical hydrology* (2nd ed.). Johns Hopkins University Press.

Huang, H., Calabrese, S., & Rodriguez-Iturbe, I. (2021). Variability of ecosystem carbon source from microbial respiration is controlled by rainfall dynamics. *Proceedings of the US National Academy of Sciences*, *118*(52), e2115283118. https://doi.org/10.1073/pnas.2115283118

Kostka, J. E., Dalton, D. D., Skelton, H., Dollhopf, S., & Stucki, J. W. (2002). Growth of Iron(III)-reducing bacteria on clay minerals as the sole electron acceptor and comparison of growth yields on a variety of oxidized iron forms. *Applied and Environmental Microbiology*, *68*(12), 6256–6262. https://doi.org/10.1128/AEM.68.12.6256-6262.2002

Laio, F., Porporato, A., Ridolfi, L., & Rodriguez-Iturbe, I. (2001). Plants in water-controlled ecosystems: Active role in hydrologic processes and response to water stress. *Advances in Water Resources*, *24*(7), 707–723. https://doi.org/10.1016/S0309-1708(01)00005-7

Lovley, D. R. (1991). Dissimilatory Fe(III) and Mn(IV) reduction. *Microbiological Reviews*, *55*(2), 259–287. https://doi.org/10.1128/mr.55.2.259-287.1991

Maggi, F., Gu, C., Riley, W. J., Hornberger, G. M., Venterea, R. T., Xu, T., et al. (2008). A mechanistic treatment of the dominant soil nitrogen cycling processes: Model development, testing, and application: Nitrogen cycle modeling. *Journal of Geophysical Research*, *113*(G2), G02016. https://doi.org/10.1029/2007JG000578

Magnabosco, C., Lin, L.-H., Dong, H., Bomberg, M., Ghiorse, W., Stan-Lotter, H., et al. (2018). The biomass and biodiversity of the continental subsurface. *Nature Geoscience*, *11*(10), 707–717. https://doi.org/10.1038/s41561-018-0221-6

Manzoni, S., & Porporato, A. (2007). A theoretical analysis of nonlinearities and feedbacks in soil carbon and nitrogen cycles. *Soil Biology and Biochemistry*, *39*(7), 1542–1556. https://doi.org/10.1016/j.soilbio.2007.01.006

Manzoni, S., & Porporato, A. (2009). Soil carbon and nitrogen mineralization: Theory and models across scales. *Soil Biology and Biochemistry*, *41*(7), 1355–1379. https://doi.org/10.1016/j.soilbio.2009.02.031

Miele, F., Benettin, P., Wang, S., Retti, I., Asadollahi, M., Frutschi, M., et al. (2022). Dataset—Spatially explicit linkages between redox potential cycles and soil moisture fluctuations. *Zenodo*. https://doi.org/10.5281/zenodo.6407290

Moyano, F. E., Vasilyeva, N., Bouckaert, L., Cook, F., Craine, J., Curiel Yuste, J., et al. (2012). The moisture response of soil heterotrophic respiration: Interaction with soil properties. *Biogeosciences*, *9*(3), 1173–1182. https://doi.org/10.5194/bg-9-1173-2012

Murray, J. D. (2002). *Mathematical biology* (3rd ed.). Springer.

Nakao, H., & Mikhailov, A. S. (2010). Turing patterns in network-organized activator–inhibitor systems. *Nature Physics*, 6(7), 544–550. https://doi.org/10.1038/nphys1651

Peiffer, S., Klemm, O., Pecher, K., & Hollerung, R. (1992). Redox measurements in aqueous solutions—A theoretical approach to data interpretation, based on electrode kinetics. *Journal of Contaminant Hydrology*, *10*(1), 1–18. https://doi.org/10.1016/0169-7722(92)90041-C

Porporato, A., & Yin, J. (2022). *Ecohydrology dynamics of life and water in the critical zone*. Cambridge University Press.

Queloz, P., Bertuzzo, E., Carraro, L., Botter, G., Miglietta, F., Rao, P., & Rinaldo, A. (2015). Transport of fluorobenzoate tracers in a vegetated hydrologic control volume: 1. Experimental results. *Water Resources Research*, *51*(4), 2773–2792. https://doi.org/10.1002/2014wr016433

Ray, R., & Nyle, C. (2017). *The nature and properties of soils* (15th ed.). Pearson Press.

Richaume, A., Angle, J., & Sadowski, M. (1989). Influence of soil variables on insitu plasmid transfer from *escherichia coli* to *rhizobium fredii*. *Applied and Environmental Microbiology*, *55*(7), 1730–1734. https://doi.org/10.1128/aem.55.7.1730-1734.1989

Rillig, M. C., Mueller, L., & Lehmann, A. (2017). Soil aggregates as massively concurrent evolutionary incubators. *The ISME Journal*, *11*(9), 1943–1948. https://doi.org/10.1038/ismej.2017.56

Rinaldo, A., Benettin, P., Harman, C. J., Hrachowitz, M., McGuire, K. J., van der Velde, Y., et al. (2015). Storage selection functions: A coherent framework for quantifying how catchments store and release water and solutes. *Water Resources Research*, *51*(6), 4840–4847. https://doi.org/10.1002/2015WR017273

Rinaldo, A., Gatto, M., & Rodriguez-Iturbe, I. (2020). *River networks as ecological corridors. Species, populations, pathogens*. Cambridge University Press.

Roden, E. E., & Wetzel, R. G. (1996). Organic carbon oxidation and suppression of methane production by microbial Fe(III) oxide reduction in vegetated and unvegetated freshwater wetland sediments. *Limnology & Oceanography*, *41*(8), 1733–1748. https://doi.org/10.4319/lo.1996.41.8.1733

Rodríguez-Escales, P., Barba, C., Sanchez-Vila, X., Jacques, D., & Folch, A. (2020). Coupling flow, heat, and reactive transport modeling to reproduce in Situ redox potential evolution: Application to an infiltration pond. *Environmental Science & Technology*, *54*(19), 12092–12101. https://doi.org/10.1021/acs.est.0c03056

Rodriguez-Iturbe, I., Cox, D., & Isham, V. (1987). Some models for rainfall based on stochastic point processes. *Proceedings of the Royal Society of London A*, *410*, 269–288.

Rodriguez-Iturbe, I., & Porporato, A. (2005). Ecohydrology of water-controlled ecosystems. In *Soil moisture and plant dynamics*. Cambridge University Press.

Roels, J. A. (1980). Application of macroscopic principles to microbial metabolism. *Biotechnology and Bioengineering*, *22*(12), 2457–2514. https://doi.org/10.1002/bit.260221202

Rubol, S., Manzoni, S., Bellin, A., & Porporato, A. (2013). Modeling soil moisture and oxygen effects on soil biogeochemical cycles including dissimilatory nitrate reduction to ammonium (DNRA). *Advances in Water Resources*, *62*, 106–124. https://doi.org/10.1016/j.advwatres.2013.09.016

Scheidweiler, D., Miele, F., Peter, H., Battin, T. J., & de Anna, P. (2020). Trait-specific dispersal of bacteria in heterogeneous porous environments: From pore to porous medium scale. *Journal of The Royal Society Interface*, *17*(164), 20200046. https://doi.org/10.1098/rsif.2020.0046

Schroth, G., Kolbe, D., Pity, B., & Zech, W. (1995). Searching for criteria for the selection of efficient tree species for fallow improvement, with special reference to carbon and nitrogen. *Fertilizer Research*, *42*(1–3), 297–314. https://doi.org/10.1007/BF00750522

Simkus, D., Slater, G., Sherwood-Lollar, B., Wilkie, K., Kieft, T., Magnabosco, C., et al. (2016). Variations in microbial carbon sources and cycling in the deep continental subsurface. *Geochimica Cosmochimica Acta*, *173*(10), 264–283. https://doi.org/10.1016/j.gca.2015.10.003

Šimůnek, J., & Suarez, D. L. (1993). Modeling of carbon dioxide transport and production in soil: 1. Model development. *Water Resources Research*, *29*(2), 487–497. https://doi.org/10.1029/92WR02225

Šimůnek, J., van Genuchten, M., & Šejna, M. (2012). Hydrus: Model use, calibration, and validation. *Transactions of the American Society of Agricultural and Biological Engineers*, *55*(4), 1261–1274.

Soucy, S., Huang, J., & Gogarten, J. (2015). Horizontal gene transfer: Building the web of life. *Nature Reviews Genetics*, *16*(8), 472–482. https://doi.org/10.1038/ncomms12770

Stumm, W., & Morgan, J. (1996a). *Aquatic chemistry: Chemical equilibria and rates in natural waters* (3rd ed., pp. 425–515). John Wiley Sons.

Stumm, W., & Morgan, J. J. (1996b). *Aquatic chemistry: Chemical equilibria and rates in natural waters* (3rd ed.). Wiley.

Tecon, R., & Or, D. (2017). Biophysical processes supporting the diversity of microbial life in soil. *FEMS Microbiologicy Reviews*, *41*(5), 599–623. https://doi.org/10.1093/femsre/fux039

Ter Braak, C. J., & Vrugt, J. A. (2008). Differential evolution Markov chain with snooker updater and fewer chains. *Statistics and Computing*, *18*(4), 435–446. https://doi.org/10.1007/s11222-008-9104-9

Vrugt, J., ter Braak, C. J. F., Diks, C. G. H., Robinson, B. A., Hyman, J. M., & Higdon, D. (2010). Accelerating Markov chain Monte Carlo simulation by differential evolution with self-adaptive randomized subspace sampling. *International Journal of Nonlinear Sciences and Numerical Stimulation*, *10*(3), 273–290. https://doi.org/10.1515/ijnsns.2009.10.3.273

Wang, X., Liu, L., Piao, S., Janssens, I., Tang, J., Liu, W., et al. (2014). Soil respiration under climate warming: Differential response of heterotrophic and autotrophic respiration. *Global Change Biology*, *20*(10), 3229–3237. https://doi.org/10.1111/gcb.12620

Weber, K. A., Achenbach, L. A., & Coates, J. D. (2006). Microorganisms pumping iron: Anaerobic microbial iron oxidation and reduction. *Nature Reviews Microbiology*, *4*(10), 752–764. https://doi.org/10.1038/nrmicro1490

Yan, Z., Bond-Lamberty, B., Todd-Brown, K., Bailey, V., Li, S., & Liu, C. (2018). A moisture function of soil heterotrophic respiration that incorporates microscale processes. *Nature Communications*, *9*(1), 2652. https://doi.org/10.1038/s41467-018-04971-6

Yan, Z., Liu, C., Todd-Brown, K. E., Liu, Y., Bond-Lamberty, B., & Bailey, V. L. (2016). Pore-scale investigation on the response of heterotrophic respiration to moisture conditions in heterogeneous soils. *Biogeochemistry*, *131*(1–2), 121–134. https://doi.org/10.1007/s10533-016-0270-0

Zhang, Z., & Furman, A. (2021). Soil redox dynamics under dynamic hydrologic regimes - a review. *Science of the Total Environment*, *763*, 143026. https://doi.org/10.1016/j.scitotenv.2020.143026

Erratum

The originally published version of this article omitted some author contributions. Mitra Asadollahi should be added to Data curation, Formal analysis, and Investigation. The errors have been corrected, and this may be considered the authoritative version of record.